FOI

A Study of Dynamic Properties of S355J2 Steel and Y925 Tungsten Alloy

GENG SHENG WANG

FOI-R--4941--SE
ISSN 1650-1942 March 2021

Geng Sheng Wang

A Study of Dynamic Properties of S355J2 Steel and Y925 Tungsten Alloy

Titel	A Study of Dynamic Properties of S355J2 Steel and Y925 Tungsten Alloy
Title	En studie om dynamiska och brottegenskap av S355J2 stål och Y925 volframlegering
Rapportnr/Report no	FOI-R--4941--SE
Månad/Month	March
Utgivningsår/Year	2021
Antal sidor/Pages	52
ISSN	1650-1942
Kund/Customer	FM
Forskningsområde	Undervattensforskning
FoT-område	Vapen och skydd
Projektnr/Project no	E60961, E60973
Godkänd av/Approved by	Henric Östmark
Ansvarig avdelning	Försvars- och säkerhetssystem

Sammanfattning

I denna studie har försök gjorts för att karakterisera de dynamiska hållfasthets- och brottegenskaperna för säkerhets- och försvarsapplikationer. För att kunna karaktärisera dynamiska hållfasthets och brottegenskaperna för S355J2 stål och Y925 volframlegering har materialprovning och hybridanalyser av provresultaten genomfört. Aktiviteten inkluderar konstruktion av provstavar och metod för materialprov. Numeriska analys och en systemmetod utvecklas för att kunna analysera dynamiska provresultat vid hög belastningshastighet. Med hjälp av enstångs drag-Hopkinson och multistänger-Kosky-anläggning visas att pålitliga materialprov kan genomförs med komplexa provkropparna. Metoder att identifiera kritiska materialparametrar för olika brottsmönster har studerats. Med metoder har parametra för avancerade brottmodell framtagna för ballistiska tillämpningar. Med hybridmaterialprovmetod har parametrar för Johnson-Cook-hållfast och brottmodeller bestämts och validerats för hög töjnings-hastighet och temperatureffekten. Vidare utförs karaktärisering av en mer avancerade brottmodell, Hosford-Mohr-Coulombs modell baserat på den framtagna provmetoden.

Nyckelord: S355J2, Y925, mekaniska egenskap, töjnings-hastighet, brottmekanik, temperatur, Hosford-Coulomb, Johnson-Cook, materialprov, flytgräns.

Summary

In this study, efforts have been made to characterize the dynamic strength and failure properties of S355J2 steel and Y925 alloy for security and defence applications. Material tests and hybrid analyses of the results have been performed. The activity includes both the design of tests and analyses of the results. A simulation based method to analyse dynamic test results is developed for high strain rate tests using the Hopkinson single bar impactor and Kosky split bar apparatus. With the help of the system method, it is shown that material parameters can be identified with tailor made specimens for specific material model. The critical values for different failure patterns are determined for different material models for ballistic applications when the high strain rate impulse load and adiabatic heating are important considerations. The study includes complex fracture patterns that are often of a great concern. With the developed method, parameters for Johnson-Cook models for both material have been determined and validated for the effect of strain rate hardening and temperature softening. In addition, parameters for an advanced fracture model, the Hosford-Mohr-Coulomb failure models, are determined for S355J2 steel based on the material test results.

Keywords: S355J2, Y925, mechanical property, strain rate, fracture locus, Hosford-Coulomb, Johnson Cook, material tests, yield criterion.

Contents

1 Introduction

For ballistic applications, many materials show significantly different mechanical responses compared to those at quasi-static loading condition. Impulsive loads at high velocity and the adiabatic temperature change may lead to a significantly different material responses. To characterize the mechanical properties at the dynamic loading condition is essential for understanding and analysing the performance of different ballistic solutions for national security and defence applications.

Compared to the construction steels, many of the materials for the ballistic protection and penetration applications behave differently due to their specific strength and density requirements. They often have different metallurgical structures. To characterize their mechanical behaviour, advanced constitutive and fracture models have often to be considered.

In recent decades, significant advances have been made with the help of the simulation technique for the mechanical tests of various materials [1-4]. These techniques integrate numerical simulations with tailored material tests. They make it possible for the development of consistent material strength and fracture models by integrating the simulation techniques with the material test activities.

A hybrid method has been previously developed in [1] for quasi-static material tests. The method benefits from numerical simulations to determine material parameters from the tests. Furthermore, a system method is developed in [2] for the dynamic material tests. The method is developed to study not just the response of test specimens. The whole test setup is studied to determine both the material response of the specimen and the loading condition applied on the specimen. For the present study, further focus has been put on the development of methodology for the material tests at complex stress and loading conditions. These tests are essential for the development of advanced strength and fracture models for ballistic applications.

An example of the advanced fracture models, the Hosford-Mohr-Coulomb failure model is studied within this work. This fracture model is based on Mohr-Coulomb frictional failure model. The characteristics of the model is discussed, and various material testing methods are explored to determine parameters for this model.

Two different materials; a conventional construction steel, S355J2, and a hard tungsten alloy, Y925, are studied with respect to their strength as well as the fracture behaviour. The study is based on the previous studies on the mechanical properties of S355J2 steel, as given in [1] and [3] for the strain hardening, and as given in [2] and [4] for the strain rate hardening and the failure characteristics [1].

Even though some studies have been performed for the mechanical properties of Y925 as given in [5-6], further material tests have been performed to verify the consistency for a new batch of material. Additional material parameters at the complex stress state and high strain rate at different temperatures are determined for the parameters for the advanced models.

The additional tests have been performed to provide additional material data for the loading and failure patterns relevant to ballistic applications. For example, tailored material tests for the shear load and for the failure due to stress concentrations etc., have been performed to determine the corresponding material parameters.

The purpose is both to validate the results from previous studies and to implement new test routines to determine parameters of various material models. New parameters are determined from the tests for the development of advanced failure models. This report provides improved sets of parameters for the mechanical properties of S355J2 and Y925 alloys for the yield model. In addition, the fracture model based on the advanced Hosford-Mohr-Coulomb (HMC) fracture model has been studied for S355J2 steel.

2 General Stress condition

Some basic concepts are reviewed in this section to help to understand advanced material models based on the solid mechanics considerations.

Generally, the stress condition at any material point in a solid may be fully determined by three stress invariants. These invariants are independent of the stress directions. For the ordered principle stresses for $\sigma_1 > \sigma_2 > \sigma_3$, the stress invariants are defined by:

$$I_1 = \sigma_1 + \sigma_2 + \sigma_3 \tag{1}$$

$$J_2 = \frac{1}{6}[(\sigma_1 - \sigma_2)^2 + (\sigma_2 - \sigma_3)^2 + (\sigma_3 - \sigma_1)^2] = \frac{1}{3}\sigma_{VM}^2 \tag{2}$$

$$J_3 = (\sigma_1 - \sigma_m)(\sigma_2 - \sigma_m)(\sigma_3 - \sigma_m) \tag{3}$$

Accordingly, the stress at each point in a solid is fully defined with its coordinates in the Cartesian stress space with the axis of the ordered principle stresses.

By definition, the mean stress is a quantity to characterize the internal pressure ($p = -\sigma_m$) that is determined with the first stress invariant of I_1:

$$\sigma_m = \frac{I_1}{3} = \frac{1}{3}(\sigma_1 + \sigma_2 + \sigma_3) \tag{4}$$

The von Mises equivalent stress is determined with the second stress invariant of J_2:

$$\sigma_{VM} = \sqrt{3J_2} = \left\{\frac{1}{2}[(\sigma_1 - \sigma_2)^2 + (\sigma_2 - \sigma_3)^2 + (\sigma_3 - \sigma_1)^2]\right\}^{1/2} \tag{5}$$

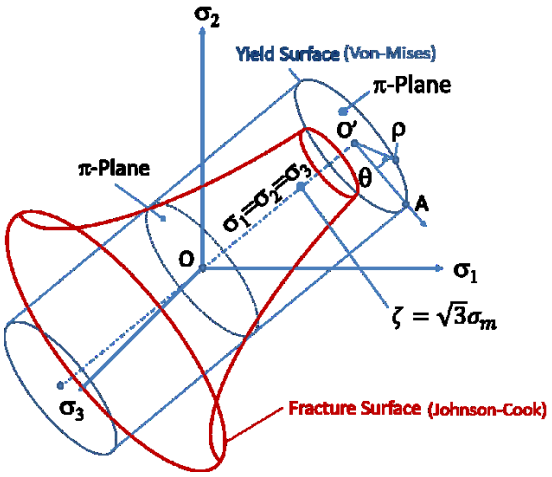

Figure 1: Schematic of the stress space, Cartesian coordinates of order principle stresses, and idealized yield vs fracture surfaces characterized in Haigh–Westergaard coordinates

The Lode parameter [7], is determined by both the second and the third stress invariant J_3, as a dimensionless parameter of:

$$\xi = \frac{3\sqrt{3}}{2}\frac{J_3}{J_2^{3/2}} = \frac{27}{2}\frac{(\sigma_1-\sigma_m)(\sigma_2-\sigma_m)(\sigma_3-\sigma_m)}{\sigma_{VM}^3} \tag{6}$$

The stress triaxiality is determined as a dimensionless parameter η by the first and second stress invariant:

$$\eta = \frac{\sigma_m}{\bar{\sigma}_{VM}} = \frac{I_1}{3\sqrt{3J_2}} \tag{7}$$

For the shear dependent materials, Haigh–Westergaard coordinates is often a convenient space for the characterization of material properties. This is a polar coordinates

perpendicular to the pressure axis in the Cartesian stress space as shown in Fig.1. In the coordinates, $\bar{\theta}$ is the so-called Lode angle parameter determined by:

$$\bar{\theta} = 1 - \frac{2}{\pi} cos^{-1}(\xi) \quad (8)$$

The equivalent shear stress is determined with the polar length ρ, see Fig.1, for a value defined by the second stress invariant J_2:

$$\rho = \sqrt{2J_2} = \sqrt{\frac{2}{3}}\sigma_{VM} \quad (9)$$

3 Yield surface

The plastic yield differs from the elastic deformation in that the deformation will convert the strain energy to the plastic work. For many homogenous materials, the shear based yield criterion is often a good approximation. This criterion omits the contribution of internal pressure to the yield of the material.

After the yield, the volume of the material may be assumed to be constant, independent of the pressure. The shear stress is considered to be a dominant yield driving force. Obviously, this assumption may not be valid when the material undergoes significant change in volume after the yield. Gases, porous materials etc., for example, will change in volume under pressure. In addition when the material is subjected to the detonation load, the incompressible assumption of the material after the yield may not be valid for many materials.

The simplest shear criteria is the Tresca yield criterion. This criterion assumes that the maximum shear stress will determine the yield of a material. The Tresca yield condition can be expressed with an equivalent maximum shear stress defined by the principle stresses:

$$\bar{\sigma}_{Tresca} = \frac{1}{2}[|\sigma_1 - \sigma_2| + |\sigma_2 - \sigma_3| + |\sigma_3 - \sigma_1|] \quad (10)$$

The plastic deformation will consume deformation energy, this dictates that the expansion of the yield surface should be concave. A mathematically simple yield surface is the von-Mises yield surface. The yield is assumed to occur when the von Mises equivalent stress reaches a certain constant, independent of both the pressure (σ_m), the first stress invariant, and Lode parameter (ξ), the third stress invariant:

$$\bar{\sigma}_{VM} = \sqrt{3J_2} = const. \quad (11)$$

To assume the yield value of σ_{VM} to be the same for a complex stress state as that for a simple one-dimensional tension one, a similarity principle may bridge one dimensional material test results to complex three dimensional yield conditions.

To bridge Tresca and von-Mises yield criteria, Hosford has proposed a general equivalent yield stress surface. The Hosford isotropic yield criterion [8] is a generalized yield surface defined by:

$$\bar{\sigma}_{HF} = \left\{\frac{1}{2}\left[|\sigma_1 - \sigma_2|^a + |\sigma_2 - \sigma_3|^a + |\sigma_3 - \sigma_1|^a\right]\right\}^{1/a} \quad (12)$$

The stress $\bar{\sigma}_{HF}$ becomes Tresca shear stress for $a = 1$ (Eq. (10)), and von Mises shear stress for $a = 2$ (Eq. (5)). A general concave yield surface may be constructed by limiting the parameter to $1 \leq a \leq 2$.

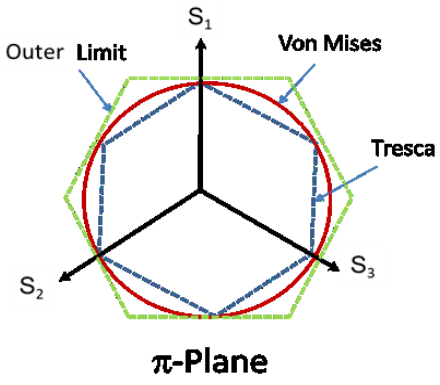

Figure 2: Comparison of various yield surface assumptions in Haigh–Westergaard coordinates in the π-Plane

To illustrate the yield models, Fig.2 compares some yield assumptions in the π -plane in the Haigh–Westergaard coordinates as shown in Fig.1. For a general isotropic yield assumption, the Lode parameter (the polar angle in Fig.2) will affect the yield criterion (the polar length), except for the von Mises yield model which is independent of the Lode angle with respect to the shear invariants (a constant polar length along the principle stress deviator S_1, S_2, and S_3).

Compared to the von Mises yielding condition, the yield value for Tresca criterion at the shear condition will become:

$$\left(\bar{\sigma}_y\right)_{Tresca} = \left(\bar{\sigma}_y\right)_{VM} \cos\left(\frac{\pi}{6}\right) = 0.866\left(\bar{\sigma}_y\right)_{VM} \quad (13)$$

The yield stress from the Tresca yield assumption will be 13.4% lower for the shear condition than that from the von Mises yield assumption. Near fracture for many metallic materials, there will generally be a significant difference in the values of the critical strain even for a small change in the stress, since the gradient of the stress with respect to the plastic strain may often become very small. A slightly different yield stress may lead to a significant difference for the value of critical strain.

4 Strain hardening

During the yield, part of the deformation energy is converted to the permanent plastic deformation. After the initial plastic yield, a change in the value of yield may occur. Many metallic materials exhibit a strain hardening behavior during the plastic deformation. The strain hardening indicates an increased yield stress when further plastic deformation occurs. Elastic perfectly-plastic material is a limit example when a material may lose its plastic stability when yield occurs.

Strain hardening has been observed for many materials so that an increased load is needed to create further plastic deformation. For ballistic applications, a widely used model is the Johnson-Cook strength model [9]. This model approximates the plastic hardening with an empirical equation:

$$\sigma_y\left(\varepsilon_p, \dot{\varepsilon}_p, T\right) = \left[A + B\left(\varepsilon_p\right)^n\right][1 + Cln(\dot{\varepsilon}^*)][1 - (T^*)^m] \quad (14)$$

This model accounts for, empirically, effects of strain hardening and strain rate effect as well as the temperature softening of a material. In this equation, σ_y is an equivalent (von-Mises) yield stress, ε_p is the equivalent plastic strain. $\dot{\varepsilon}^*$ and T^* is normalized strain rate and temperature. The normalized strain rate is defined by:

$$\dot{\varepsilon}^* = \frac{\dot{\varepsilon}}{\dot{\varepsilon}_0} \quad (15)$$

Here, $\dot{\varepsilon}_0$ is a reference strain rate. Often, $\dot{\varepsilon}_0 = 1\ s^{-1}$ is assumed for convenience. With some computational codes, however, one has to be very careful about this value. The implementation in the computational code may use this reference strain rate as a cut-off value so that the strain rate coefficient C is assumed to be $C = 0$ for the strain rate $\dot{\varepsilon} < \dot{\varepsilon}_0$, even though there may be still a considerable difference in the strength of the material between the quasi-static loading condition and the reference loading condition at the strain rate of $\dot{\varepsilon}_0 = 1\ s^{-1}$.

To account for the temperature effect, a normalized value is defined by:

$$T^* = \frac{T - T_r}{T_m - T_r} \quad (16)$$

Here, T_r is a reference temperature, often the room temperature at which the mechanical property of the material is tested. T_m is the melt temperature of the material, simply used to approximate the zero shear strength when a material begins to change its state from solid to liquid. Again for the temperature less than the reference one, the temperature softening effect must be carefully considered especially for the value of m other than 1.

When the stress is reversed after the yield, a material may initially behave elastically, similar to the initial condition. At a higher reversed stress, reversed yield may occur at the similar initial yield stress level. This is often called an isotropic hardening. However, many materials may exhibit a so called “Baushinger” effect so that the yield at the reversed load will occur at different values than the initial ones, see the left hand side of Fig.3 for which a von Mises yield model is shown.

On the π-plane as shown in Fig.3, the isotropic hardening is represented by an expanding yield surface around the center while for kinematic hardening, the yield surface is not just expanded, the center of the yield surface will move as well, depending on the loading direction. A so-called “back stress” vector is usually used to determine the location of the center of the newly created yield surface.

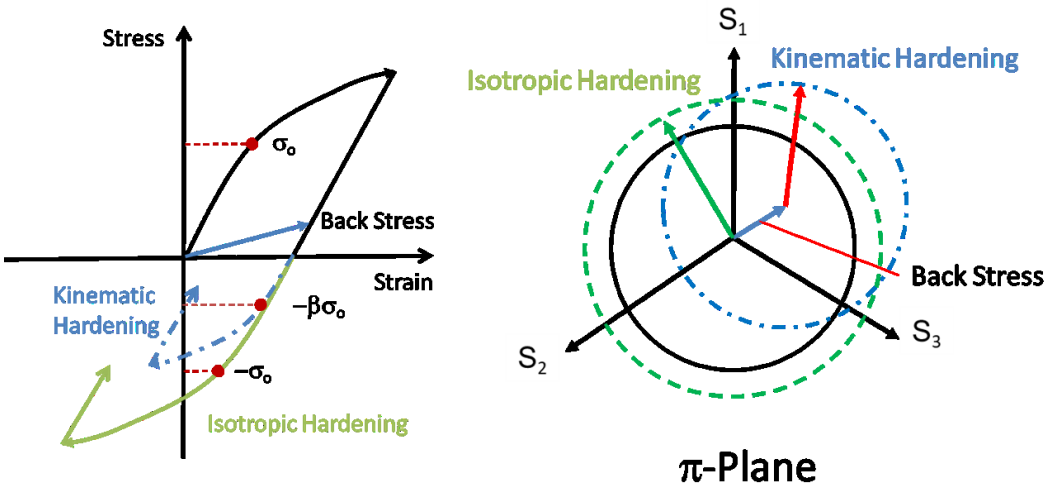

Figure 3: Schematic of the comparison of various strain hardening behaviors in the stress space

5 Failure models

For most metallic materials, the shear stress may be considered to be the major driving force for both the yield and failure. It is often assumed that a material may fail when the shear stress reaches a critical value. Since von Mises stress represents a homogeneous equivalent shear stress, the simplest failure criterion is to assume a critical value of the von Mises stress. This value can be simply determined from the tension tests with smooth specimens. While a constant von Mises failure stress is simple to apply and adequate for many applications, more advanced failure criterion will often be needed for advanced ballistic applications.

A widely used failure model for ballistic applications is the phenomenal Johnson-Cook fracture model [10] that is an extension of the strength model as given in Eq. (14) for the value of the critical equivalent failure strain instead. This model is expressed as:

$$\varepsilon_f^p = (D_1 + D_2 e^{D_3 \eta})(1 + D_4 ln|\dot{\varepsilon}^*|)(1 + D_5 T^*) \quad (17)$$

The failure model is based on the observation of fracture strains of some metallic materials that show a strong dependency for the failure strain on the internal pressure.

To account for the effect of internal pressure on the failure strain, the triaxiality parameter η is considered. This is the value of mean stress normalized with the von Mises stress (Eq. (7)). The empirical failure model of Eq.(17) is expected to be able to account for the experimental observation that many materials may exhibit much less critical value of failure strain when a strong three dimensional constraint is presented. For example in the tests using notched specimens, the critical failure strain will often become significantly smaller than that when a smooth specimen is used.

In recent years, many research works ([11-13]) based on advanced numerical simulations showed that the failure models such as the Johnson-Cook model (Eq.17) have become increasingly inadequate for many of the ballistic applications. The shortcoming becomes increasingly obvious for the complex problems such as high velocity fragmentations and penetrations. Particularly when the high strength and high density materials are considered. Use of Eq. (17) often results in unsatisfactory results. Use of more advanced models may result in a much better prediction of the material responses.

One of the successful failure models is the Mohr-Coulomb based model [14]. This model recognizes the effect of the normal pressure on a shear plane. The effect of normal pressure on the shear strength is assumed in a linear manner. According to this model, the failure will occur on a shear plane when the maximum combined value of the shear stress (τ) and normal stress (σ_n) reaches a critical value (c_2):

$$max(\tau + c_1 \sigma_n) = c_2 \quad (18)$$

This is a straight forward assumption. For a critical shear value of c_2, the Mohr-Coulomb factor of c_1 will determine how the normal stress σ_n on the shear plane may affect the critical shear stress. This model is sometimes called the frictional shear failure model since the constant c_1 acts like the friction coefficient in the Coulomb friction model. This relation assumes that a compressive pressure on a shear plane will increase the critical shear stress, while a tension in the normal direction of the shear plane will reduce the critical shear stress. This is a first order approximation of the effect of the normal stress on a shear plane to the critical shear stress.

At a plane stress condition, a schematic of the frictional model is shown in Fig.4, in comparison to some other fracture models. It is shown that this frictional model will be able to account for asymmetric material strength in tension and compression. The model accounts for the strength of the material that is dependent on the orientation of the stress. It will have different strengths for uniaxial tension, shear, compression, and a general combination of the stress.

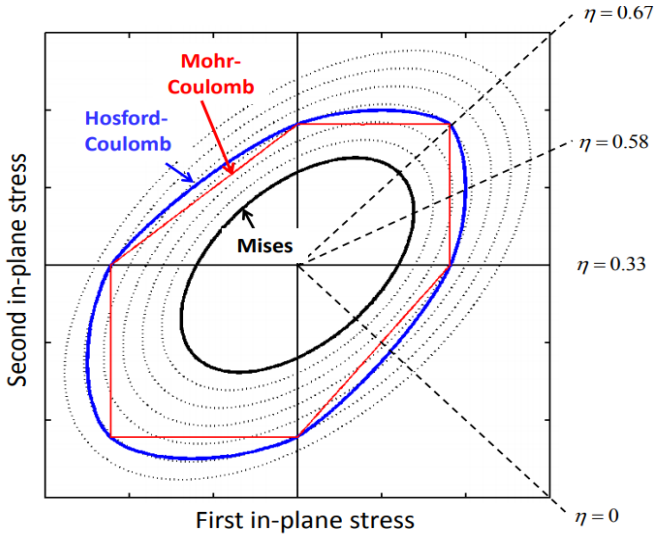

Figure 4: Comparison of different failure criteria at the critical condition for a complex stress state

To assume the failure to occur at the maximum shear plane, the maximization has an analytical solution which is given by a solution of the quantity for the ordered principal stresses:

$$(\sigma_1 - \sigma_3) + c(\sigma_1 + \sigma_3) = b \tag{19}$$

This solution relates to the coefficients of the Mohr-Coulomb model as given in Eq. (18) such as:

$$c = \frac{c_1}{\sqrt{1+c_1^2}} \tag{20}$$

The parameter is determined by a friction coefficient c_1. The constant b is related to the model of Eq. (18) such that:

$$b = \frac{2c_2}{\sqrt{1+c_1^2}} \tag{21}$$

In this relation, $(\sigma_1 - \sigma_3)$ is the maximum shear stress (the Tresca stress), the stress as given in Eq. (10):

$$\bar{\sigma}_{Tresca} = \sigma_1 - \sigma_3 \tag{22}$$

The Mohr-Coulomb model may as well be written as:

$$\bar{\sigma}_{Tresca} + c(\sigma_1 + \sigma_3) = b \tag{23}$$

This failure model is a function of not just the maximum shear stress ($\bar{\sigma}_{Tresca}$), but also includes the effect of the maximum stress σ_1 and the minimum stress σ_3.

To replace Tresca (maximum shear) stress with a more general Hosford stress as given in Eq. (12), the failure model may be rewritten as, [15]:

$$\bar{\sigma}_{HF} + c(\sigma_1 + \sigma_3) = b \tag{24}$$

This assumption results in a more general failure surface that is an extension of the Mohr-Coulomb failure surface (Tresca failure) as compared schematically in Fig.4. As a comparison in this figure, the von Mises failure surface is shown as the dashed surfaces.

A transformation from Cartesian coordinates of the ordered principle stress into Haigh–Westergaard stress coordinates gives the solutions for the principle stresses:

$$\begin{cases}\sigma_1 = \bar{\sigma}(\eta + f_1) \\ \sigma_2 = \bar{\sigma}(\eta + f_2) \\ \sigma_3 = \bar{\sigma}(\eta + f_3)\end{cases} \tag{25}$$

Where $\bar{\sigma}$ is the von Mises stress defined by Eq.(5). In these relations:

$$\begin{cases} f_1 = \frac{2}{3}cos\left[\frac{\pi}{6}(1-\bar{\theta})\right] \\ f_2 = \frac{2}{3}cos\left[\frac{\pi}{6}(3+\bar{\theta})\right] \\ f_3 = -\frac{2}{3}cos\left[\frac{\pi}{6}(1+\bar{\theta})\right]\end{cases} \tag{26}$$

where η is the stress triaxiality parameter defined by Eq. (7), and $\bar{\theta}$ is the Lode angle parameter defined by Eq. (8). The Hosford-Mohr-Coulomb fracture stress is solved as:

$$\bar{\sigma}_f(\eta, \bar{\theta}) = \frac{b}{\left\{\frac{1}{2}\left[|f_1 - f_2|^a + |f_2 - f_3|^a + |f_3 - f_1|^a\right]\right\}^{1/a} + c(2\eta + f_1 + f_3)} \tag{27}$$

or

$$\bar{\sigma}_f(\eta, \bar{\theta}) = \frac{b}{g_{HC}(a,c)} \tag{28}$$

for

$$g_{HC} = \left[\frac{1}{2}\left[|f_1 - f_2|^a + |f_2 - f_3|^a + |f_3 - f_1|^a\right]\right]^{1/a} + c(2\eta + f_1 + f_3) \tag{29}$$

This is a stress based failure model that requires three constants: b, c, and a, each has its own physical interpretation.

Unlike the yield surface of Eq.(12), the exponential coefficient a in the failure model does not have to be limited between 1 and 2. There will be no energy conservation constraint for a failure model. At the event of fracture, a solid can either release or absorb strain energy.

At a uniaxial tension condition, the analytical solution for stress triaxiality is $\eta = 1/3$, and the Lode parameter is $\xi = 1$. According to Eq. (8) and Eq. (26), this leads to:

$$\bar{\theta} = 1 - \frac{2}{\pi}cos^{-1}(\xi) = 1 \tag{30}$$

and

$$\begin{cases} f_1 = \frac{2}{3} \\ f_2 = -\frac{1}{3} \\ f_3 = -\frac{1}{3}\end{cases} \tag{31}$$

According to Eq. (25), the solution for the ordered principle stresses become:

$$\begin{cases}\sigma_1 = \bar{\sigma}(\eta + f_1) = \bar{\sigma}_0 \\ \sigma_2 = \bar{\sigma}(\eta + f_2) = 0 \\ \sigma_3 = \bar{\sigma}(\eta + f_3) = 0\end{cases} \tag{32}$$

where $\bar{\sigma}_0$ is the uniaxial failure stress. These solutions give:

$$g_{HC} = 1 + c \tag{33}$$

Accordingly, the failure stress $\bar{\sigma}_0$ relates to the constants in the model by:

$$\bar{\sigma}_0 = \frac{b}{1+c} \tag{34}$$

For a failure criterion, the stress is usually not a good quantity for many materials since their stress gradient with respect to the plastic strain will often become very small near the

fracture. For the extreme case of a elastic perfectly-plastic material for example, the stress gradient is close to zero. As a result, a slight change in the stress may lead to a significant change in the plastic strain. The common practice is to adopt the fracture strain instead as a quantity to characterize the failure of the plastic materials.

At the near failure state, a power hardening law may often be adequate to relate the plastic strain to the stress. The stress as a function of strain may be simplified according to:

$$\bar{\sigma}_f = A\varepsilon_{eff}^{nf} \tag{35}$$

To assume $\varepsilon_0$as the failure strain for the uniaxial tension, Eq. (34-35) gives:

$$\bar{\sigma}_0 = \frac{b}{1+c} = A\varepsilon_0^{nf} \tag{36}$$

Dividing the failure stress of Eq. (28) by Eq. (36) gives:

$$\frac{\bar{\sigma}_f(\eta,\bar{\theta})}{\bar{\sigma}_0} = \frac{b}{g_{HC}(a,c)}\frac{1+c}{b} = \frac{A\varepsilon_{eff}^{nf}}{A\varepsilon_0^{nf}} \tag{37}$$

This gives a solution for the failure as a function of the plastic strain:

$$\bar{\varepsilon}_f = \varepsilon_0\left[\frac{1+c}{g_{HC}(a,c)}\right]^{\frac{1}{nf}} \tag{38}$$

Notice that, in addition to the strain hardening coefficient of nf from the simplified Eq. (35), the fracture model is fully determined with three constants: ε_0, the tension fracture strain for the ideal uniaxial tension load, a, the Hosford constant, and c, the Mohr-Coulomb factor.

Mathematically to determine these constants according to the test results, it will become a minimization problem of:

$$\min \sum_{i=1}^{m\geq 3}\left\{\frac{\varepsilon_0}{\bar{\varepsilon}_f^i\left(\xi_f^i,\eta_f^i\right)}\left[\frac{1+c}{g_{HC}\left(a,c,\xi_f^i,\eta_f^i\right)}\right]^{\frac{1}{n_f}} - 1\right\}^2 \quad \text{for } \varepsilon_0, a, c \tag{39}$$

where $\bar{\varepsilon}_f^i\left(\xi_f^i,\eta_f^i\right)$ is the test values of the failure strain for each specific test design for different values of Lode parameter ξ_f^i and triaxiality η_f^i. At least three different types of material tests have to be performed to fully determine the constants of the model. The optimization algorithms for these non-linear equations in many software, e.g. Matlab, may be used to determine optimal values of these constants. For a specific application, material tests may be performed to popularize the relevant area in the failure locus to ensure the failure model is relevant for the application.

In the following sections, examples of different methods are explored and various material tests are performed to determine parameters of the material models for a common construction steel S355J2, and a very different high density and strength tungsten alloy Y925.

6 S355J2 steel

Previously, researches have performed on this material and reported in [1-4]. In these studies, various efforts are made to develop methodologies and to characterize the mechanical properties more accurately based on the numerical technique. It was recognized that some of the solutions that were provided in [1] to describe the material property may sometimes lead to ambiguousness in use of the parameters. A more generalized model and further validations are needed for the characterization of this steel, especially when second order effects are considered. The material test data from [1] have been reevaluated and validated in this work. To improve the model, some new material tests are made for a more generalized solution. New tests were performed for both quasi-static and dynamic loading conditions to validate the improved models.

6.1 Strain hardening

With the hybrid method to combine the material tests and numerical simulations, piecewise linear representations of the tension test results were determined in [1]. These results are shown in Table 1.

Table 1: Piecewise representation of the quasi-static true stress as a function of true plastic strain of the tension properties of S355J2 for different material conditions

	Rolled (Plate)	Drawn (Bar)	Annealed
Plastic Strain	Stress MPa	Stress MPa	Stress MPa
0.000	415	450.0	367.3
0.023	420	583.9	371.7
0.047	515	630.5	455.8
0.067	555	658.3	491.2
0.097	605	692.0	535.4
0.217	700	786.4	619.5
0.446	800	902.4	708.0
0.795	905	1023.6	800.9
1.994	1180	1286.1	1044.3

Based on these results (Table 1), the quasi-static plastic hardening for S355J2 is approximated accordingly as:

$$\sigma_y = A + B\left(\varepsilon_p\right)^n \tag{40}$$

According to the material tests and the results from Table 1 for drawn bars, rolled sheets, and annealed conditions, an improved set of parameters for the quasi-static yield stress of the steel is determined as:

$$\sigma_y = \begin{cases} 11.2 + 754.8{\varepsilon_p}^{0.16} \text{ MPa, for annealed} \\ 12.8 + 881.0{\varepsilon_p}^{0.16} \text{ MPa, for rolled} \\ 13.1 + 883.1{\varepsilon_p}^{0.11} \text{ MPa, for drawn} \end{cases} \tag{41}$$

These parameters are created to address the accuracy issues of the original model as proposed in [2-4]. For example for the rolled plates, the comparison between Eq.(41) and experimental results is shown in Fig.5. In this figure, various experimental results are shown as the solid lines with symbols, and the strength model from [2-3] are shown in the figure as a dotted red curve. It is shown that the model from [2-3] has considerable discrepancy with the test results for the specimens with different sizes under both the

tension and compression condition. This is one of the reasons to motivate the improvement with a new set of parameters for the yield strength of S355J2 steel.

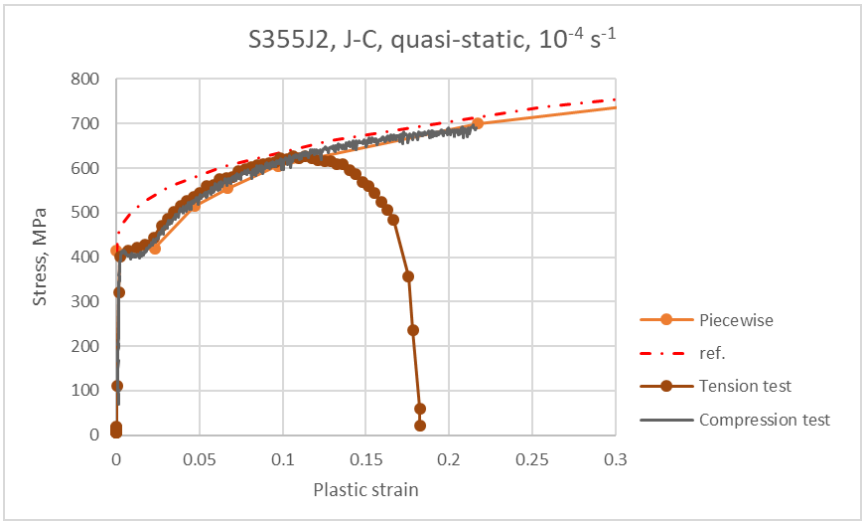

Figure 5: Johnson-Cook approximation of the quasi-static yield strength of S355J2 for the rolled plate [2-3] with various test results. In this figure, the brown curve with solid circles is from the small specimen tension test. The gray curve is from compression tests, and the orange curve with symbols is from [1]. The red dotted curve is JC model from [1]

The JC strength model is a result of compromise for the fitting of test data with the power hardening law. For the rolled plate, the model from [2-3] is shown as black dashed curves in Fig.6. The new model is shown as light blue dashed curves. To determine the yield stress after necking, different methods have been used. In [3], Bridgman's empirical method is used to determine the material data after necking in [1], while later on, an advanced hybrid method is developed to correlate the test data to material parameters.

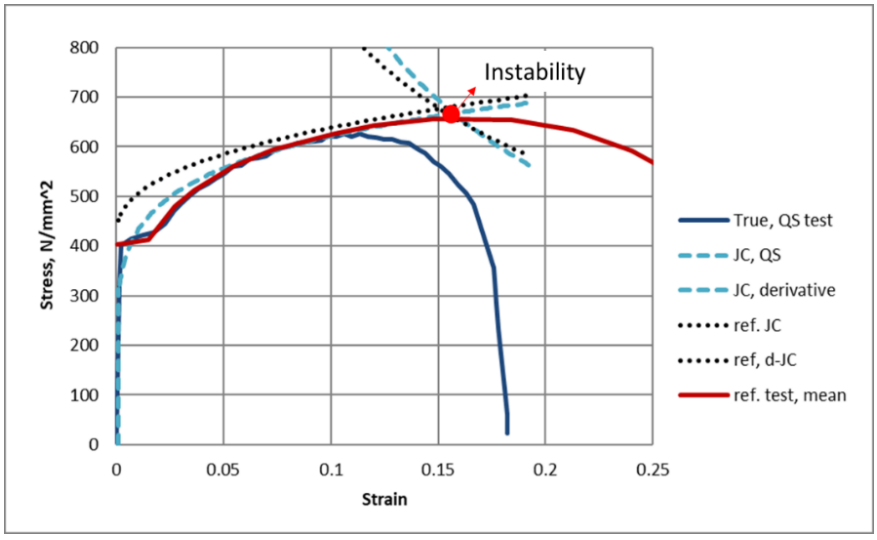

Figure 6: Johnson-Cook approximation of the quasi-static yield strength of S355J2 for the rolled plate [2-3] compared to the tension test results from different specimen sizes. The effect of necking is indicated at the cross point with the derivative of the model.

For small deformation, there is some discrepancy between the model and the test result. The reason is mainly due to approximation of the strain hardening law according to Eq. (40). This hardening law is not adequate enough to represent the whole range of the

material response. In the small plasticity range, the comparison between the test and the formulation is shown in Fig.6. It is shown that the experimental results shows a plateau for the yield stress in the beginning. This response cannot be fitted with Eq. (40).

To correctly represent the material behavior, considerations have to be made to include the first order effect to obtain a model with the least difference with the test results. Efforts have been made in the present study for a more balanced approximation of the yield for both small and large range of plastic deformation. The example is shown in Fig.6 as the blue dashed curve which shows an improved correlation to the test data for a larger range of deformation. In addition, a constraint has to be put in the hardening law to capture the initiation of geometrical instability, the necking, of the material. According to this constraint, the derivative of the yield stress with respect to the plastic strain should have a cross point in the deformation model near the maximum experimental load, see Fig.6.

6.1.1 Validation

The JC model for plastic deformation is an approximation, a compromise for simplicity and ease of use. Validations have to be made to ensure that the models will be adequate even for large plastic deformation. Since the material model will be used for numerical simulations, validation of the model from the simulation of the tension tests will become valuable to help understanding the potential of the model.

To validate the model of Eq. (41), numerical models are created based on the convergence study according to [1] with the element size controlled to be less than 0.07mm in the gauge area. Reduced integration elements are used in the model to reduce the numerical locking issues at large deformation. The small element size is necessary for converged simulation results when the material is undergoing localized large plastic deformation.

A comparison of the simulated deformation and the photos taken during the material tests [3] is shown in Fig.7 for the smooth specimen during large plastic deformation after necking is initiated. The comparison shows that the simulation does reproduce the instability behavior, but with a slightly less necking diameter compared to the experimental results. This is probably due to the excessive hardening of the model at large strain. The numerical stiffening of a heavily deformed element in the model may also contribute to the discrepancy due to the shear and pressure locking issues of the low order elements used in the simulations.

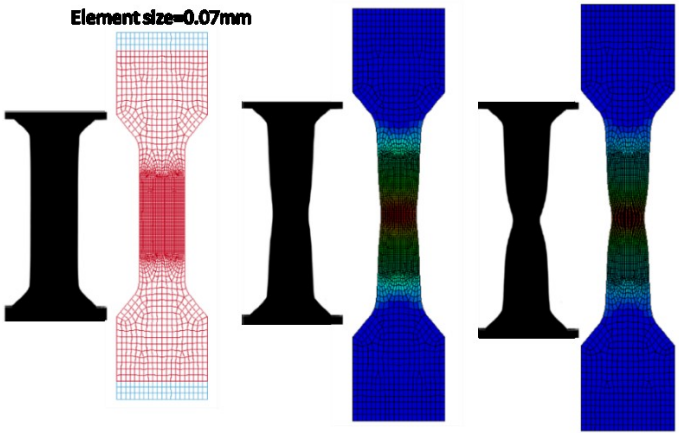

Figure 7: Comparison of the necking between the simulation and the tests

The validation are shown in Fig.8 for the load as a function of the gauge displacement. In this figure, the orange curve with symbols is the average test result. The black dashed curve is the simulation result with the new parameters (JC). The red curve is the simulation with the parameters from [3-4].

The validation shows that the previous parameters for the model, the red dashed curve, has a tendency to overestimate the material strength at small deformation, compared to the test results. The new parameters as given in Eq. (41) give an overall closer agreement to the test results. Both sets of parameters yield similar maximum load of the specimen. The prediction of instability from both models agrees well with the experimental results.

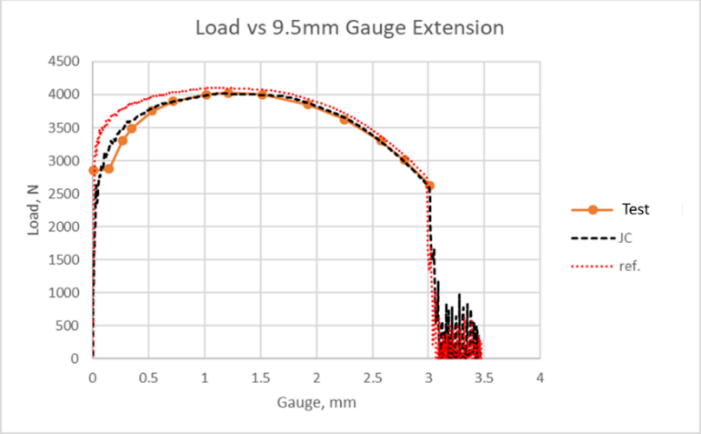

Figure 8: Validation of the parameters for the tension tests for the load as a function of the gauge displacement. "JC" is the approximation with new parameters, and "ref." is the model with parameters from [3-4]

To ensure consistency between the model and the test results, a series of tests has been performed for both quasi static loading condition, and the loading with the increased strain rate of about 3.5 1/s. For these tests, specimens with a lightly smaller diameter and a longer gauge length are used, compared to those used in [3].

A comparison of the simulation with the experimentally recorded load as a function of the gauge displacement is shown in Fig.9 for the quasi-static loading condition. For this case, two repeated tests are performed and shown in the figure as the brown curves. For comparison, the implicit simulations are performed with the original parameters from [3], shown in the figure as the red dashed curve, and the new set of parameters as given in Eq.(41), shown in the figure as the black dashed curve. The comparison shows that both models give a reasonable prediction of the instability of the specimens. However, the original model systematically overestimated the strength of the specimens, while the simulation with the new set of parameters agrees much better with the test results.

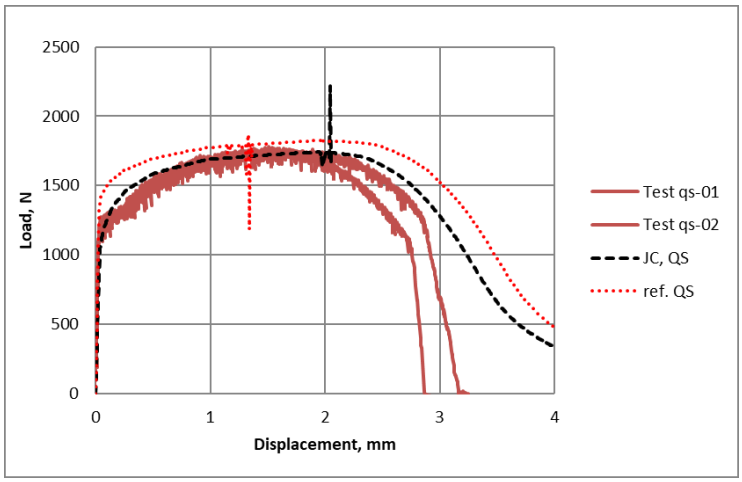

Figure 9: Comparison of different parameters for JC models for the tension tests with the smooth specimens at the quasi-static loading condition at the strain rate of $10^{-4}\ 1/s$.

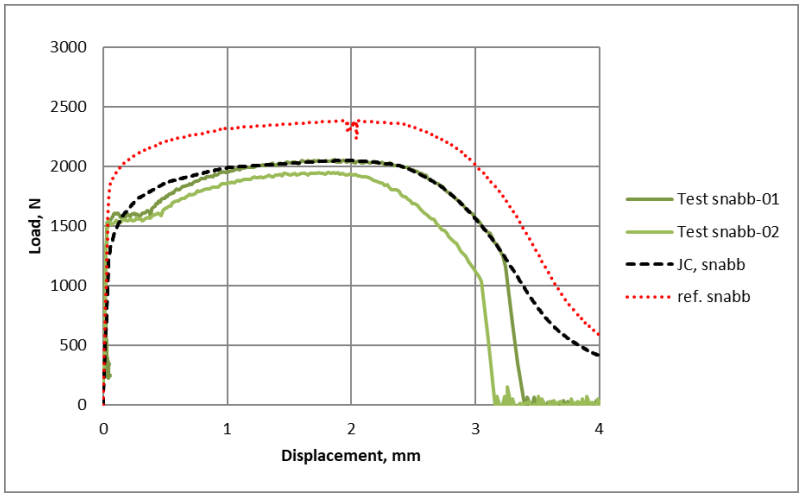

Figure 10: Comparison of different parameters for JC models for the tension tests with the smooth specimens at the elevated strain rate loading condition of 3.5 1/s

At the increased strain rate of 3.5 1/s, a comparison of the results from the tests and simulations with different parameters is shown in Fig.10 for the load as a function of the gauge displacement. Again in this figure, the simulation results according to the parameters from [3-4] is shown as the red dashed curve, and the simulations with the new parameters is shown as the black dashed curve. Apparently, the parameters for JC model from [3-4] significantly overestimates the strength of the material at this strain rate.

For the annealed and drawn condition, a different type of material tests is performed in [1]. Instead of smooth tension specimens, a notched hollow cylinder specimen is used for the tests on a bi-axial material testing machine. This specimen provides possibility for the tests with the load of tension, shear, and various combinations of tension/compression and torque. Furthermore, use of the hybrid method makes it possible to adopt a rounded notch in the gauge section to prevent unwanted angled fracture at the notch.

A geometrical description of the specimen is shown in Fig.11. Based on this geometry, a two dimensional numerical model is created as shown in Fig.12. For the numerical model, the element size is controlled in the gauge section at similar level as that used for the smooth specimen simulations (0.05 mm).

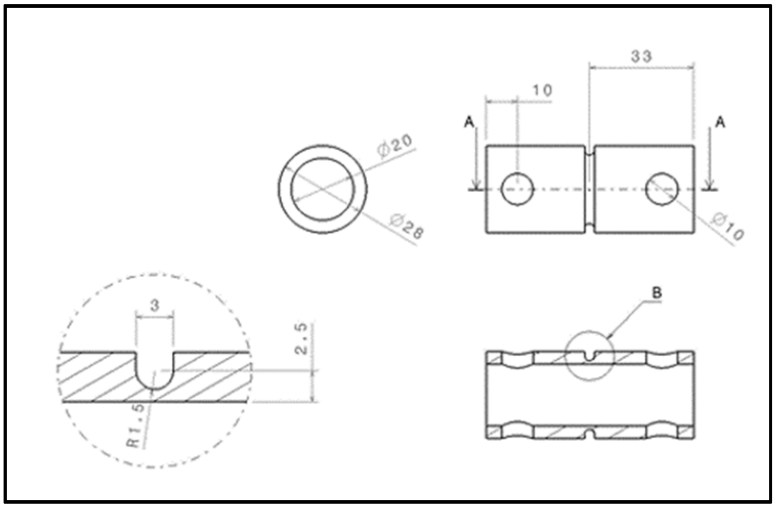

Figure 11: Geometry and dimensions of the specimen for biaxial tests for the tension, shear, and combined loading conditions.

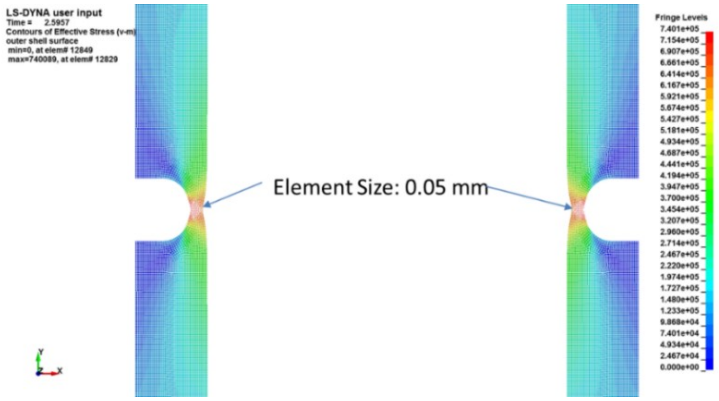

Figure 12: The numerical model of the notched test specimen for tension tests.

The validation of the strength model of Eq. (41) is shown in Fig.13 for the tension load as a function of the gauge displacement [1]. In this figure, the solid curves are the test results and the dashed curves are the simulation results. It is shown that the parameters as provided in Eq. (41) result in a reasonable agreement with the test results, especially for the values of the maximum load.

In addition to the maximum load, the critical fracture condition are identified from the simulations that result in similar failure extensions as the test results, see the comparison as shown in Fig.13. The simulations show that the tension tests with the notched specimen differ significantly in Lode parameter, compared to that of the smooth tension specimen. The test with the notched specimen will create a nearly plane strain tension condition with the Lode parameter close to zero. Interestingly for the tension load, the critical stress triaxiality is similar for both the smooth and the notched specimens. The fracture of both specimens are observed to be initiated near the center of the critical sections inside the material.

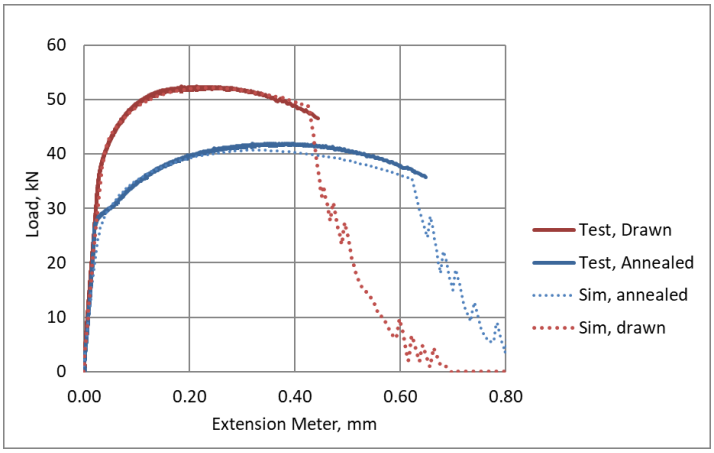

Figure 13: Validation of JC strength model and determination of failure conditions at the quasi-static loading condition.

6.1.2 Strain rate effect

For ballistic analyses, the strain rate is usually rather high and the strain rate hardening often plays a significant role in the mechanical properties of the materials. In this study, the empirical Johnson–Cook (JC) strain rate hardening constant is considered. The JC model [9], as mentioned previously is empirical and has the form as given in Eq. (14). With this model, the strain rate hardening effect is accounted for with a constant of C.

To determine this strain rate hardening constant, previous studies have been performed for S355J2 with a system method [2]. The test results are analyzed to account for the general dynamic response of the test setup [2]. The system model is used to identify the strain rate constant based on the test results. The split Hopkinson pressure bars (SHPB) apparatus is modelled in the simulations to account for the dynamic response at the measuring locations. An example of the results of the system model is shown in Fig.14 compared to the strain recordings at the incident and transmitting bar. Here, the dashed curves are the results from the simulation and the solid curves are the test measurements. The material parameter is then studied with the system model for the reflection and transmitting signals. Details of the system method is provided in [2].

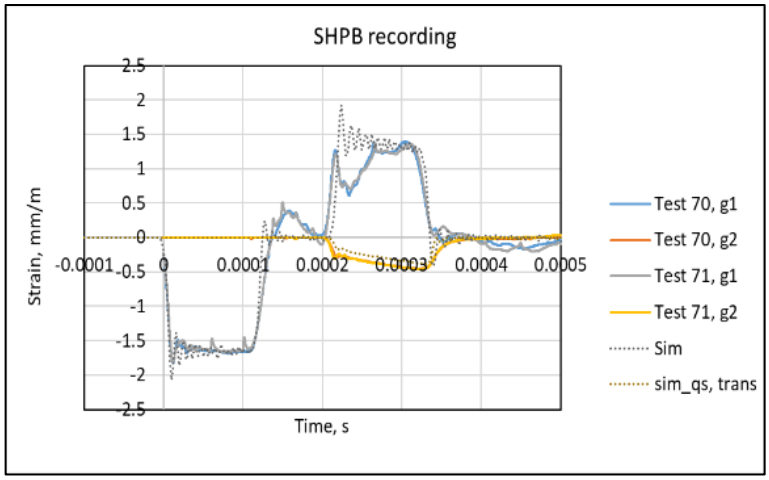

Figure 14: Comparison of simulated and measured strains from SHPB tests.

From the system model, the simulation with parameters for the quasi-static load condition are assumed to be $\dot{\varepsilon} = 10^{-4}\ s^{-1}$ and $T^* = 0$. The strain rate of $\dot{\varepsilon}_0 = 10^{-4}\ s^{-1}$ is considered as a reference. Accordingly, the quasi static strength model is expressed as:

$$\sigma_{y\_qs} = A + B\left(\varepsilon_p\right)^n \tag{42}$$

Under the dynamic loading condition for a normalized strain rate $(\dot{\varepsilon}^*)_{ref}$, the dynamic yield is determined by:

$$\sigma_{y\_dyn} = \left[A + B\left(\varepsilon_p\right)^n\right]\left[1 + C\ln\left((\dot{\varepsilon}^*)_{ref}\right)\right]\left[1 - (T^*)^m\right] \tag{43}$$

for $\dot{\varepsilon}_0 = 10^{-4}\ s^{-1}$, $T_r = 293\ K$, and $T_m = 1793\ K$. In this case, the temperature change is assumed as adiabatic, determined by:

$$\Delta T = \frac{\varphi}{\rho C_p}\int_0^{\varepsilon}\sigma(\varepsilon)\,d\varepsilon \tag{44}$$

For S355J2 steel, a constant specific heat coefficient of $C_p = 452$ J/kgK is assumed. The parameter φ is an empirical measurement of the portion of the deformation energy that is converted into heat. This parameter is often a function of the strain rate. At the impact event of a high velocity projectile or a detonation wave, this parameter is usually assumed to vary from 0.85 to 0.95 according to Meyer [16]. For the system model, a constant coefficient of $\varphi = 0.9$ is assumed.

For the given test condition, a constant DIF, the dynamic increasing factor, is defined from the simulations according to:

$$DIF = \frac{\sigma_{y\_dyn}}{\sigma_{y\_qs}} \tag{45}$$

where σ_{y_dyn} is the yield stress and σ_{y_qs} is the corresponding yield stress at the quasi-static loading condition. With an estimated strain rate $(\dot{\varepsilon}^*)_{ref}$ for the test condition, the constant C in Johnson-Cook model is determined accordingly:

$$C = \left(\frac{DIF}{[1-(T^*)^m]} - 1\right) / ln\left((\dot{\varepsilon}^*)_{ref}\right) \quad (46)$$

Several iterations of the simulations are needed before this constant is convergent to the test results.

According to the SHPB (Split-Hopkinson-Pressure-Bar) test results from [4], the simulations are performed so that the transmitting strains agree with the test measurements. The optimized results are shown in Fig.15. In this figure, the black dashed curves are the simulations and the solid curves are the test recordings. As a comparison, the simulations with the parameters from [3-4] are shown as the red dashed curves. Again, the model from [3-4] seems to significantly overestimate the strain rate hardening of the material.

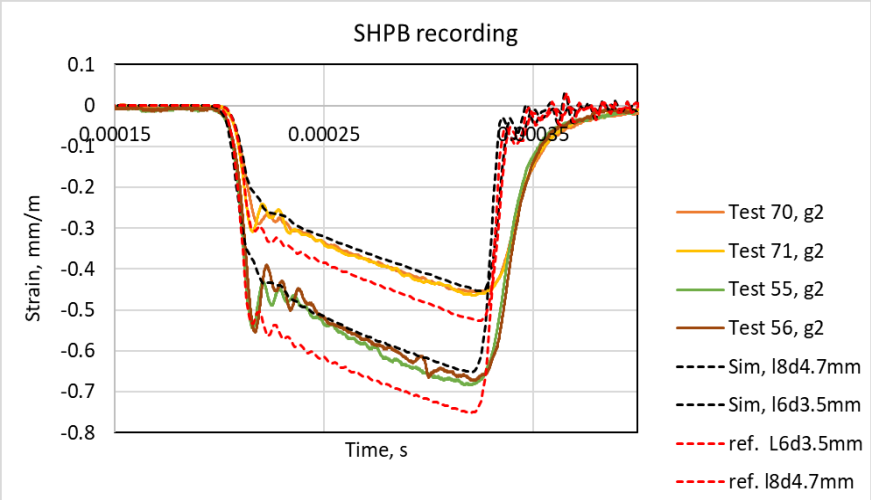

Figure 15: Validations for strain rate hardening coefficient for the simulations with the system model and the experimental measurements, at the strain rate of 3000 1/s

To further validate the model, a series of tests has been performed with a pendulum impactor single bar Hopkinson test apparatus [18]. While the SHPB apparatus provides a loading condition with the strain rate in the order of $10^3\ s^{-1}$, the pendulum apparatus can generate a strain rate in an order of $10^2\ s^{-1}$, which is between the tests with the hydraulic universal testing machine (Fig.10), and the tests with SHPB apparatus.

Again, the system method as developed in [2] are used to analyze the test results for the strain recordings on the Hopkinson bar. A comparison of the simulation results and the test recordings are shown in Fig.16. In this figure, the test strain recordings are shown as solid curves and the simulation results are shown as dashed curves.

As a comparison, the simulation with the parameters from [3-4] is shown in the figure as the red dashed curve. Again, the use of these parameters significantly overestimates the strain rate hardening of the material at the intermediate strain rate.

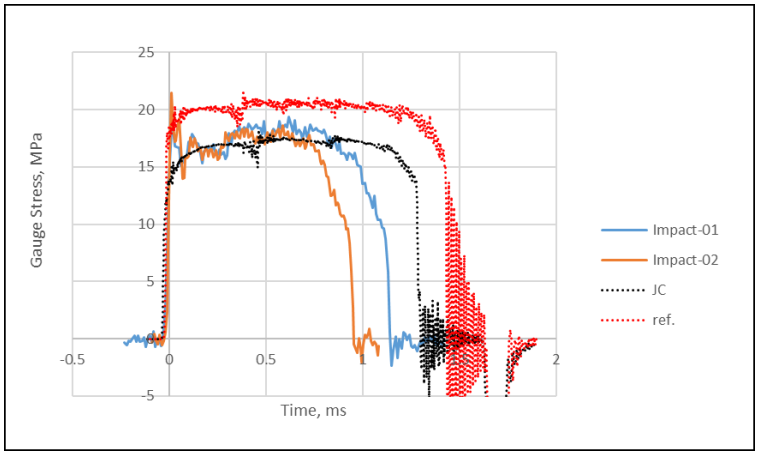

Figure 16: Comparison of the test recordings and the simulation results from the pendulum impactor Hopkinson tests at the strain rate of 300 1/s

With the hybrid method, the dynamic increasing factors (DIF) are identified for different strain rate. The results are shown in Fig.17 for the DIF as a function of strain rate. In this figure, the dashed line with symbols are estimated values according to the comparison of the test results of the maximum loads. The orange line are the strain rate hardening determined from the system model. Notice that the orange line is constrained at a value of one at the strain rate of $10^{-4}\ s^{-1}$.

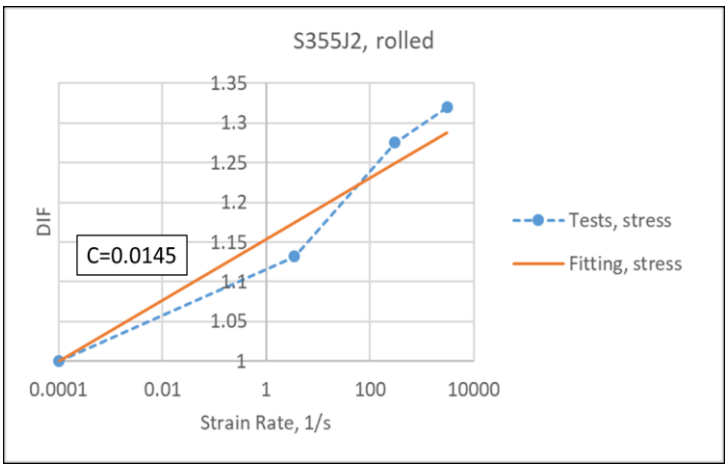

Figure 17: Comparison of the test and the simulation results for the DIF as a function of the strain rate.

According to the simulations of SHPB and pendulum impactor tests, DIF for S355J2 rolled condition is determined from the recorded transmitting strain as the verifications shown in Fig.15-16. In these figures, the test results from two different specimen sizes are compared to the model. It is shown that a strain rate hardening coefficient C=0.0145 results in a rather satisfactory agreement between the simulations and the test results. Compared to the strain rate constant as given in [2] that is based on the engineering method and a different assumption for the reference strain rate, the present coefficient is considered to be an improvement for the estimation of the strain rate hardening of S355J2 steel. It should be mentioned that the new value is significantly different from those from [1] (0.04) and [4] (0.029 for a different reference strain rate).

6.1.3 JC strength model

With the strain rate hardening constant and the thermal softening coefficient determined from [17], generalized parameters for Johnson-Cook strength model of S355J2 are determined in Eq. (47). For other material conditions, corresponding parameters may be estimated according to, for example, a reference to the hardness test of the material.

With these parameters, the reference strain rate is assumed to be $\dot{\varepsilon}_0 = 10^{-4}\ s^{-1}$. The strength model of S355J2 includes the effects of strain rate hardening and temperature softening. The yield stress is determined with the plastic strain, the strain rate, and the temperature according to Eq. (47). As validated, these new parameters will generally result in a better agreement between simulations and test data, compared to those from [1, 3-4].

$$\sigma_y = \left\{ \begin{matrix} 11.2 + 754.8{\varepsilon_p}^{0.16}\ \text{MPa, for annealed} \\ 12.8 + 881.0{\varepsilon_p}^{0.16}\ \text{MPa, for rolled} \\ 13.1 + 883.1{\varepsilon_p}^{0.11}\ \text{MPa, for drawn} \end{matrix} \right\} [1 + 0.0145\ln(|\dot{\varepsilon}^*|)][1 - (T^*)^{1.1}] \quad (47)$$

6.2 Fracture model

As discussed previously, an advanced fracture model should include the fracture conditions that are relevant to applications. For ballistic applications, for example, the stress and failure patterns are often complex. In some cases, shear failure, for example, may become more dominant than tension failure.

With the possibility to control the axial and torque load, the use of a hollow notched specimen as shown in Fig.11 makes it possible to create a shear dominant failure with application of a torque load. It is also possible to create a combined failure condition when the axial load is applied together with the torque load. In the following sections, the quasi-static experimental results for different loading conditions for S355J2 are presented.

6.2.1 Material tests

As given in details in [1], two different material conditions are tested: one for the annealed condition, and the other for the drawn condition. The tests have been performed for the shear load when only the torque is applied to the specimens until failure occurs. The rotation in the gauge section is recorded with a pair of clip gauges. The recording is used to calibrate the rotation of the hydraulic actuator for the large rotation angles. A further load is tested for which an axial compression load is applied to the specimen before the torque load begins. The magnitude of the axial load is determined according to the tension test results so that there will be no significant yield due to the axial load. The axial load will be kept constant during the torque loading.

For the annealed material condition, the experimental results of torque as a function rotational angle at the gauge section is shown in Fig.18 for the pure shear compared to the compression/shear combined loading condition. These experimental results show that the torque moment will be significantly affected by the axial load.

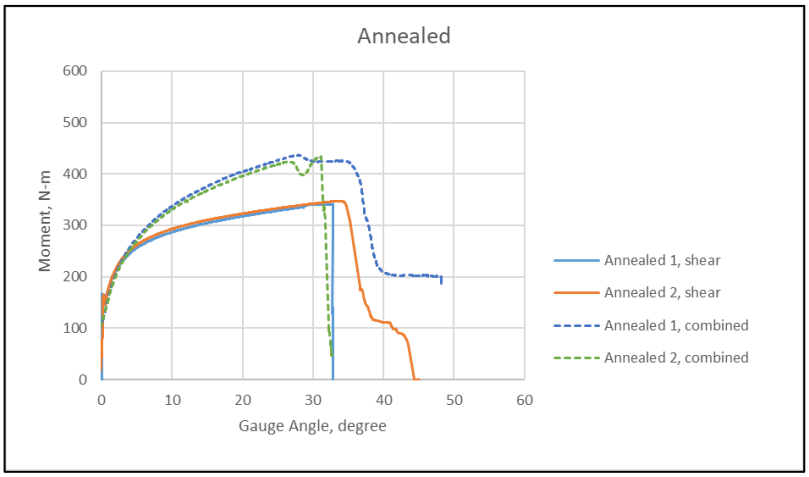

Figure 18: The test results of the torque moment at a function of the gauge rotation angle for the pure torque and combined loading condition for annealed S355J2.

For the drawn material condition, a comparison of the torque as a function of the rotational angle is shown in Fig.19. In this case, it is shown that the axial load will have a slightly less effect on the torque moment while the critical failure angle will become significantly larger when an axial compression is applied to the specimen.

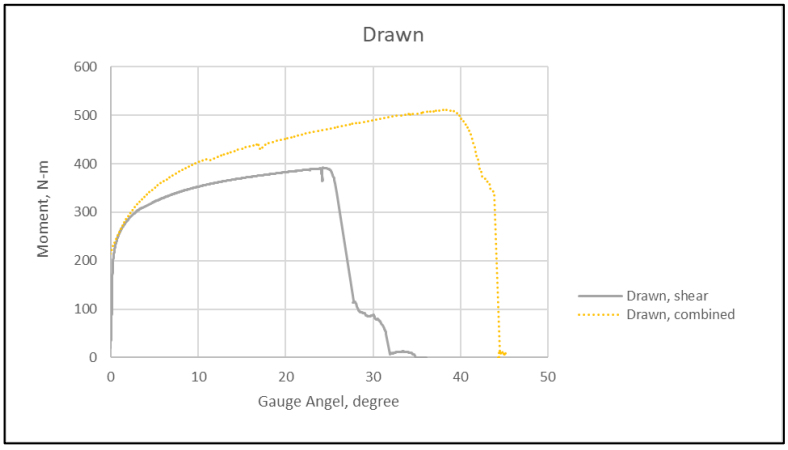

Figure 19: Comparison of the experimental torque as a function of rotation angle for the quasi-static loading condition between the shear and combined loading cases for the specimens in drawn condition

To validate the parameters for the strength model and to determine the failure conditions for tension, torque and combined loading condition, a solid model is created for the simulations. The finite element model is shown in Fig.20. This model has the finest mesh size of about 0.15 mm in the critical section. Since the simulation with a solid model requires significantly more computational resources, an increase in the element size becomes necessary so that the simulations may be performed within limited resource.

At the shear condition, the plastic deformation will become excessive. The simulations with reduced integration formulation result in significant artificial stiffening as the analyses in [1] shown. This could significantly affect the evaluation of the strain hardening and the value of critical strain. To reduce the artificial stiffening and improve the

simulation accuracy, fully integration and high accurate formulation (FORM=-2 in LS-DYNA) is used in the model.

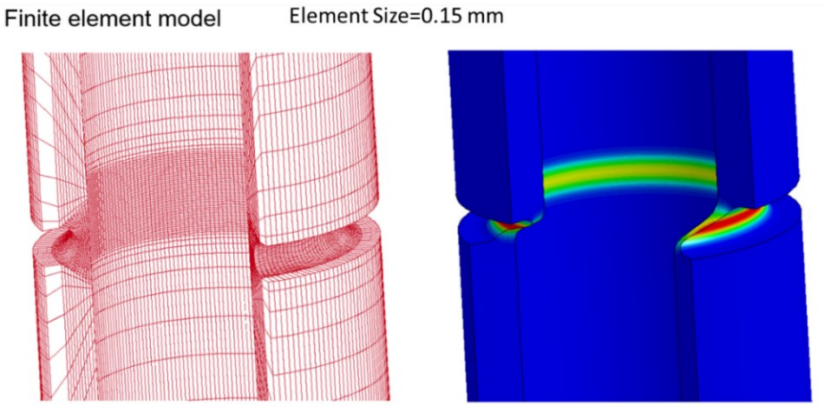

Figure 20: The finite element model for the hollow notched specimens for the shear and combined load conditions

Simulations for the tension tests are performed according to the parameters for the quasi-static strength model of Eq. (41). For the simulations, the von Mises yield mode is used. To validate the computational model, comparisons have been made between the simulations with two and three dimensional models. The results are compared in Fig.21 for the load as a function of the displacement in the gauge section. It is shown that the three dimensional model retains good consistency with the two dimensional model with finer mesh.

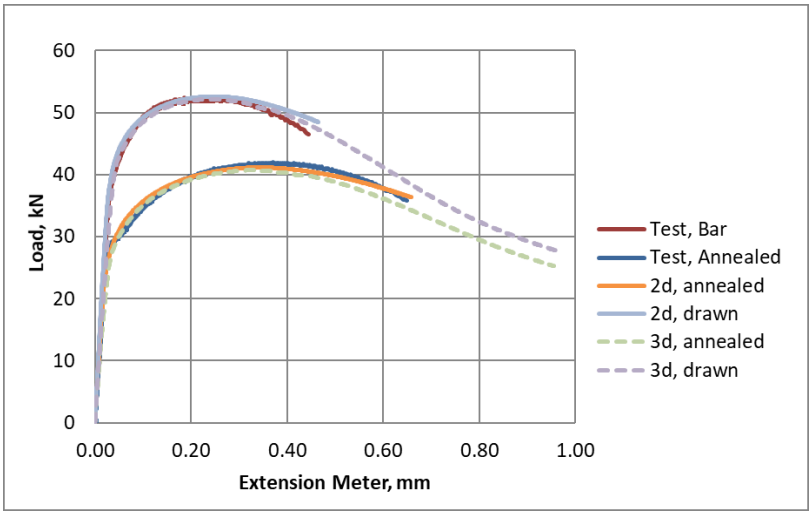

Figure 21: Comparison of the 2D and 3D simulations based on the JC strength model and von Mises yield criterion for the load as a function of the gauge displacement, together with the test results

For the pure shear [1] load, the simulated torque as a function of the rotation angle is compared in Fig.22 with the test results. In this figure, the solid curves are the test results. The dashed curves are the simulation results. The implicit simulations show an overall good agreement with the test results at the shear condition for both the annealed and drawn material condition.

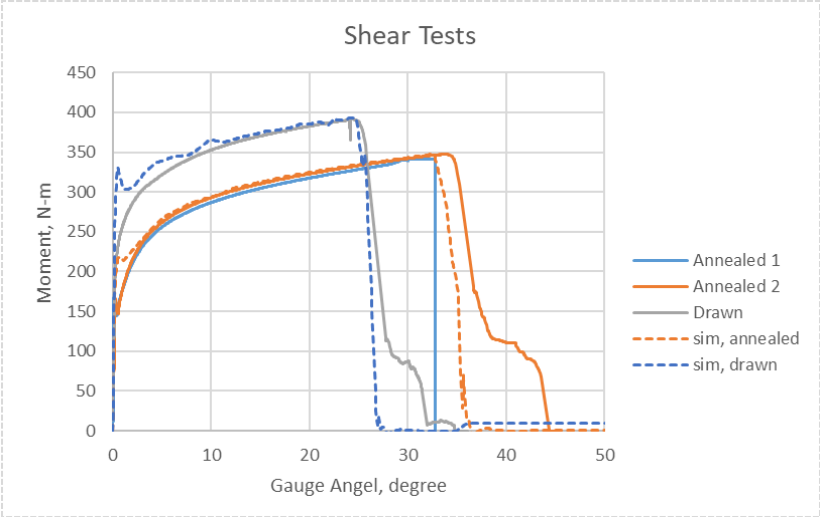

Figure 22: Comparison of the simulations based on the JC strength and von Mises yield model for the torque as a function of the rotation angle with the shear test results

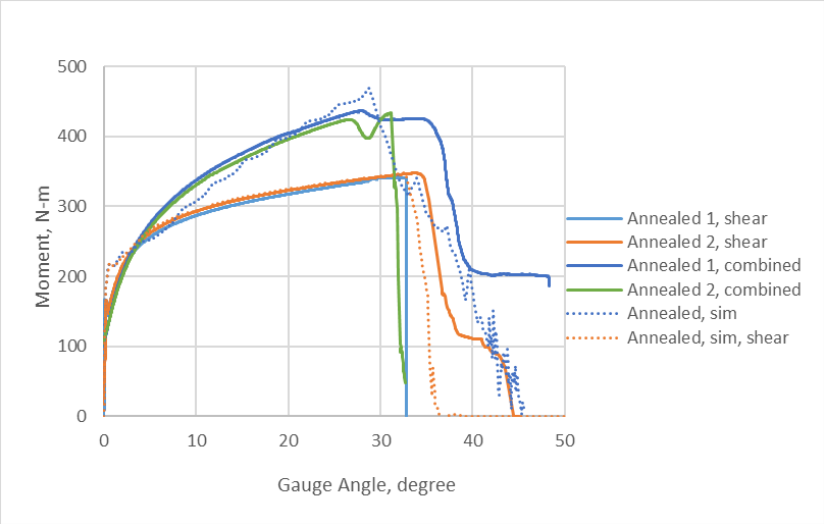

Figure 23: Comparison of the simulations based on the JC strength model and von Mises yield model for the torque as a function of the rotation angle, together with the test results for the combined loading condition

For the combined loading condition, the comparison is shown in Fig.23 for the annealed material for the pure shear and combined loading condition. Again, the simulations shows a good correlation for the torque as a function of the rotation angle under the combined loading condition. The increase in torque is shown when an axial compressive load is applied. This is an indication of the interaction between normal pressure and the torque moment, which agrees in trend with the basic Mohr-Coulomb frictional assumption, see the comparison as shown in Fig.23.

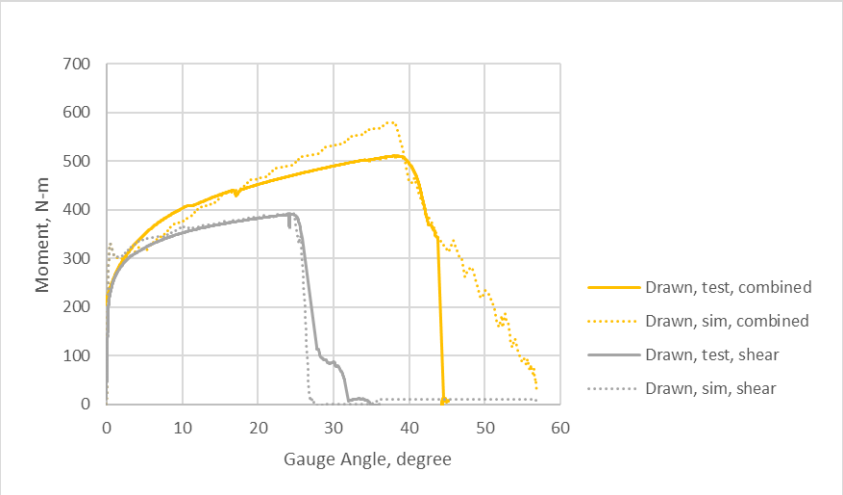

Figure 24: The effect of axial compression on the reaction torque as a function of the gauge rotation angle; experiments compared to simulations for the drawn condition

For the combined loading condition, a comparison is shown in Fig.24 for the drawn material condition for the torque as a function of the rotation angle. As shown in the comparison, the simulations have a good correlation for the torque as a function of the rotation angle under the combined load condition. The increase in torque load is observed when an axial compressive load is applied. This is an indication of the interaction between normal pressure and the torque moment for this material condition. For this material condition, the axial compression has a much more profound effect on both the torque and the failure angle.

Consequently, it is shown that the von-Mises yield surface is a very good approximation for the plastic yield of S355J2, even for different material conditions.

6.2.2 HMC model for S355J2

To determine parameters for the Hosford-Mohr-Coulomb (HMC) fracture model, the minimum should include the fracture conditions for at least three significantly different stress states, Eq. (39). Preferably, the stress should be representative for the applications. In addition to tension, shear is another important failure pattern for ballistic analyses. For the analyses of the failure of large sheets, the plane strain condition will also become an important consideration. Under the plane strain condition, use of hollow specimens provides the test results for the tension, shear, and the combinations of both the compression and shear condition.

With the hybrid method, the failure condition for the plane strain tension, the shear, and the compression/shear is identified. The results for the values of the critical failure strains are shown in Table 2 for the annealed and drawn material condition. In this table, the equivalent fracture strains and the corresponding stress conditions are provided.

Table 2: Failure conditions for S355J2 according to the hybrid method from the test of hollow notched specimens

Annealed				
ε_f	ξ	η	n_f	*Test*
0.843	0.06	0.628	0.16	Tension
2.99	0.0609	0.0168	0.16	Shear
3.5	-0.6	-0.3	0.16	Combined

Drawn				
ε_f	ξ	η	n_f	*Test*
0.639	0.0628	0.626	0.11	Tension
2.57	0.025	0.01	0.11	Shear
3.6	-1	-0.26	0.11	Combined

To determine parameters for HMC failure model, the plastic hardening parameter nf should be determined according to Eq. (35). To find a best fit according to the strength model, the hardening exponential in Eq. (35) is determined. The comparison in Fig.25 shows the best fit for the power hardening law to JC strength model of Eq. (47) for the plastic strain up to a very large value of 5. The parameters for the power law are shown in the insert of Fig.25. Accordingly, a hardening coefficient $nf = 0.16$ is determined for the annealed material condition. For the drawn condition, $nf = 0.11$ will lead to the best fit, see the comparison as shown in Fig.25.

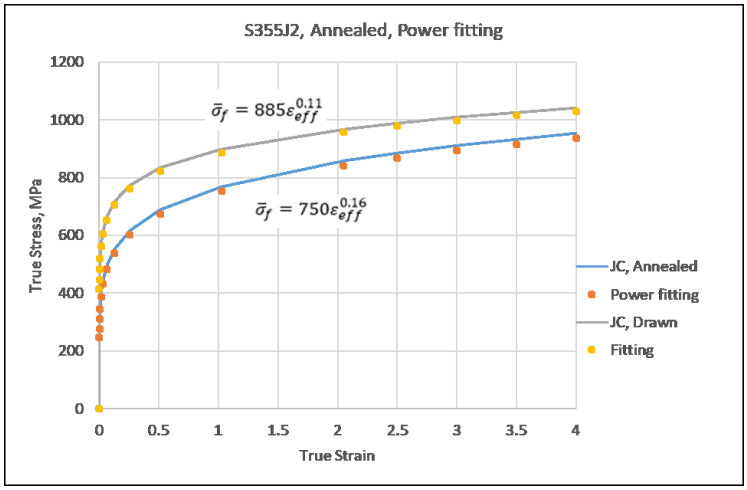

Figure 25: Fitting of the plastic hardening with the power law for the annealed and drawn material condition

Together with parameters from Table 2, the failure locus of HMC model for the annealed condition is determined according to the minimization of the nonlinear equations of Eq. (39). The resulting HMC parameters for Eq. (38) is shown in the insert of Fig.26. In this figure, the failure strain is expressed as a function of both the Lode parameter and the stress triaxiality. Similar to the Johnson-Cook failure model, the failure strain will increase significantly when stress triaxiality become low and the pressure in the material increases. For the annealed condition, the HMC failure model shows that the critical strain is about 1.015 for the uniaxial tension condition. The Mohr-Coulomb constant becomes $c = 0.12$.

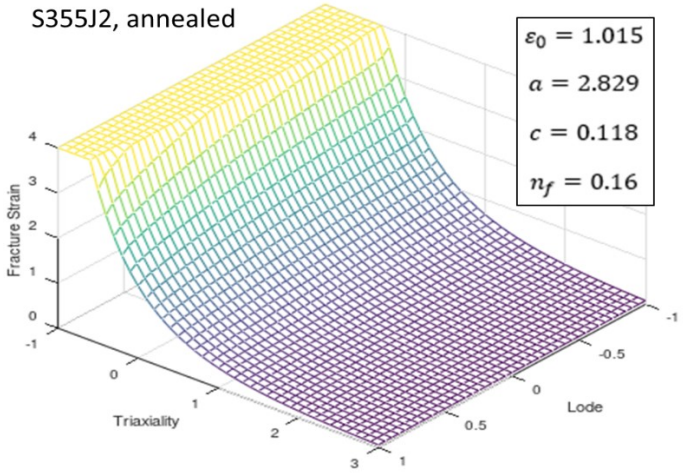

Figure 26: HMC fracture locus for S355J2 at the annealed condition.

Similarly, parameters for HMC failure model for the drawn material is determined and shown in Fig.27, with the HMC constants as shown in the insert. Compared to the annealed condition, the difference seems to be mainly in the value of uniaxial tension fracture strain ε_0 which is about 36% lower for the drawn condition, compared to that of the annealed condition. The Mohr-Coulomb factor becomes slightly lower, indicating a weaker frictional effect for this material condition.

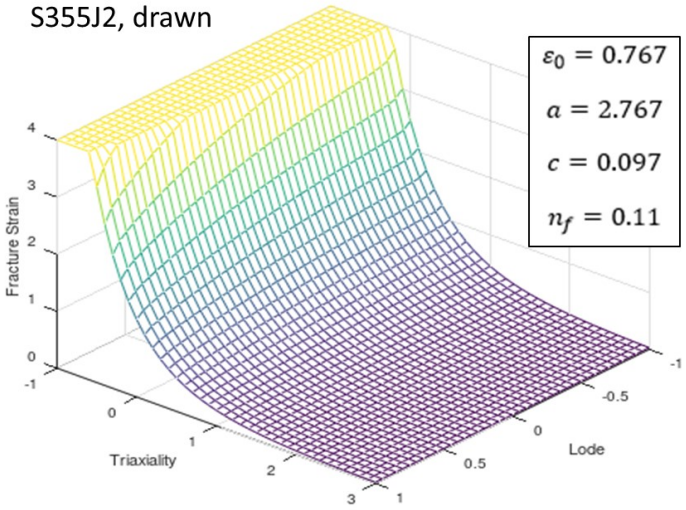

Figure 27: HMC fracture locus and constants for S355J2 in the drawn condition

6.2.3 JC equivalent failure

To determine parameters for JC failure model, tension tests with notched specimens of different notch radius are often performed. These specimens limit the Lode parameter to be nearly one when the initiation of the failure occurs at the center of the specimen. The notch radius determines the value of stress triaxiality. The resulting model is valid for the tension dominant failure pattern.

According to the HMC model, nevertheless, an equivalent JC model can be defined by assuming the Lode parameter equals to one.

JC fracture model for the quasi-static loading condition has a general form of:

$$\varepsilon_f^p = (d_1 + d_2 e^{D_3 \eta}) \quad (48)$$

for which the failure plastic strain ε_f^p is related to the stress triaxiality η with constants d_1, d_2, and D_3. These constants can be determined by a best fit to Eq. (48) for the HMC failure strain at the Lode parameter of one.

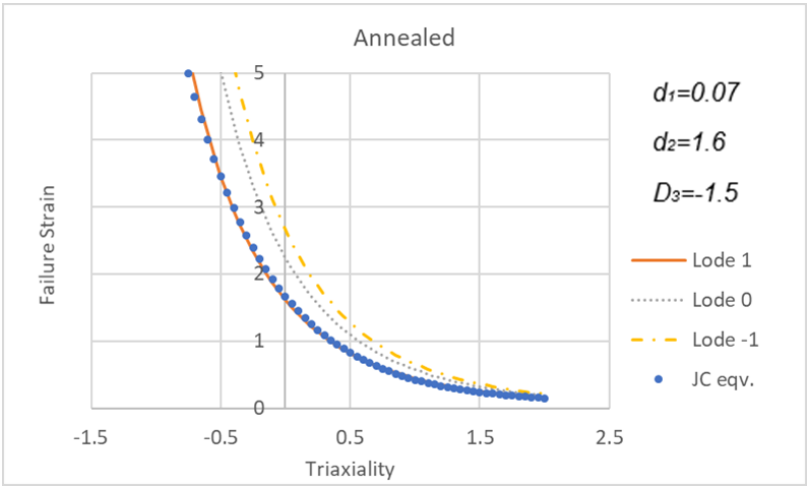

Figure 28: Comparison of HMC failure strain for various different Lode parameters for annealed condition with the equivalent JC failure parameters in the insert.

Based on the HMC locus for the annealed condition, the JC equivalent failure model for the annealed condition becomes (at room temperature and quasi-static load condition):

$$\varepsilon_f^p = (0.07 + 1.6e^{-1.5\eta}), \text{annealed} \quad (49)$$

This equivalent failure model is determined by the best fit to the HMC model for Lode=1 as the comparison in Fig.28 shows.

Similarly for the drawn condition, a comparison of the HMC failure strain as a function of stress triaxiality is shown in Fig.29 for the Lode parameters of 1, 0, and -1. Again, the behavior is similar. The equivalent JC constants for the quasi-static load is shown in the insert. For this material condition, there is a larger difference in the failure strain between tension failure (Lode=1) and the shear failure (Lode=0), compared to that for the annealed condition.

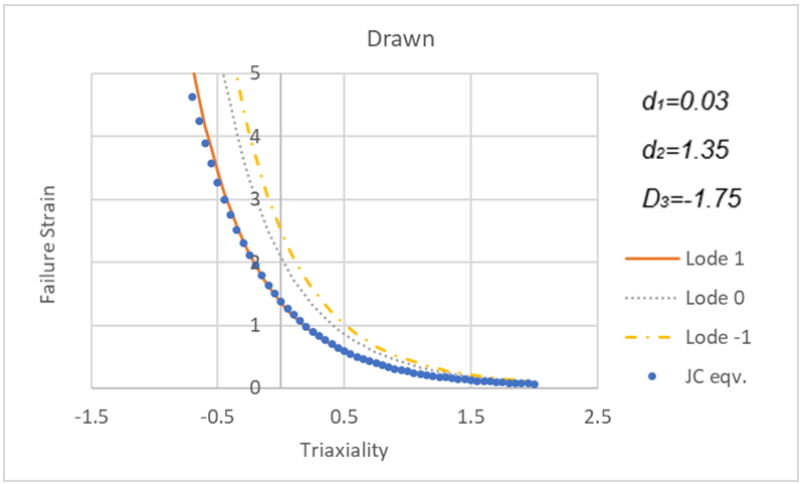

Figure 29: Comparison of HMC failure strain for various Lode parameters for the drawn condition.

The parameters for the equivalent JC failure model for the drawn condition becomes:

$$\varepsilon_f^p = (0.03 + 1.35e^{-1.75\eta}), \text{drawn} \quad (50)$$

No material tests has been performed for the rolled condition with the hollow notched specimens. Therefore, its HMC model is not determined. Since the mechanical property for the rolled condition seems to be between those of the annealed and drawn condition, an averaged equivalent JC model may be used for failure model of the rolled condition. A comparison of the estimated JC model for these material conditions is shown in Fig.30. In this figure, the value for the rolled condition is the mean value of the annealed and the drawn condition. Moreover, the failure strain for the smooth specimen tension test from [1] is shown as a red solid triangle symbol in this figure, compared to the JC models. Even through the failure strain from the smooth specimen seems to be higher than the estimated mean value, it is still slightly lower than that for the annealed condition.

.

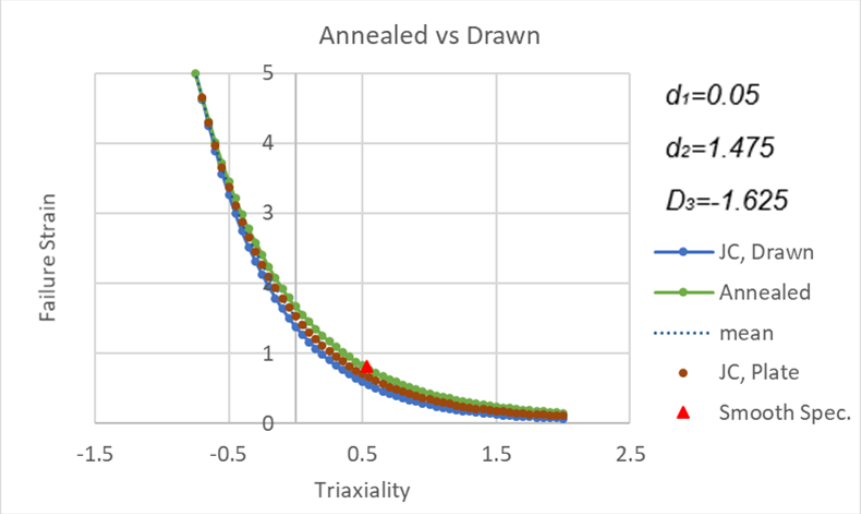

Figure 30: Comparison of JC failure models for different material conditions

The estimated JC failure model for the rolled condition becomes:

$$\varepsilon_f^p = (0.05 + 1.475e^{-1.625\eta}), \text{rolled} \quad (51)$$

This model results in a slightly lower fracture strain, compared to the tests with the smooth specimens as shown in Fig.30 as the solid red triangle symbol. It is considered to be conservative.

7 Y925 tungsten alloy

There have been several investigations for the similar alloys previously [5], including the original work by Johnson and Cook [9]. There appeared to be discrepancies in the parameters between the results by these investigators [5, 9]. In addition, there is still a need for a validated and consistent fracture model for this alloy. Y925 represents a material with high strength, Young's modulus, and density. The available size of the raw material for the material tests is small. It is included in this report to highlight the material testing methodology for the tests with small specimens.

To validate the strength model and develop an advanced failure model, various material tests have been made. In this section, the results of these efforts are summarized together with the development of the parameters for JC strength model.

7.1 Material tests

To validate the strength model, a new set of tests have been performed at quasi-static and accelerated load rate. The single bar Hopkinson impact tests [18] have been performed for higher strain rate. Some of the tension tests have been performed at elevated temperatures up to 1500 ºC.

For the tension tests, a smooth specimen design is used, similar to the tests of S355J2. The dimension of the specimen is shown in Fig.31. The specimen has a diameter of 2 mm in the gauge section. Clip gauge extensometer are used in the gauge section during the quasi-static loading to measure the extension of the specimen as a function of the load. The measurement from the extensometer gives an important reference to correlate the displacement of the load cell to the displacement in the gauge section. This specimen has an extended gauge section to comply the test standard for the elongation parameter of A5 with a 10 mm gauge distance.

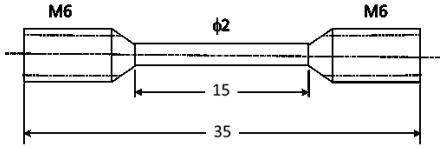

Figure 31: Dimensions of the smooth tension specimen for the tension tests of Y925

With a universal material testing machine (MTS 250kN), repeated tests for at least three specimens for each loading condition were performed. At the quasi-static tension loading condition, the loading rate is controlled so that the strain rate is about 10^{-4} s^{-1} (denoted as "qs" in the figures). For the dynamic test on this hydraulic servo machine, the loading rate is increased up to 3.5 s^{-1} (denoted as "snabb" in the figures), which is almost the upper limit of the loading capability of the testing machine.

A comparison of the test results is shown in Fig.32 for the quasi-static load as well as the load at accelerated velocity. In this figure, the engineering stress is expressed as a function of the engineering strain.

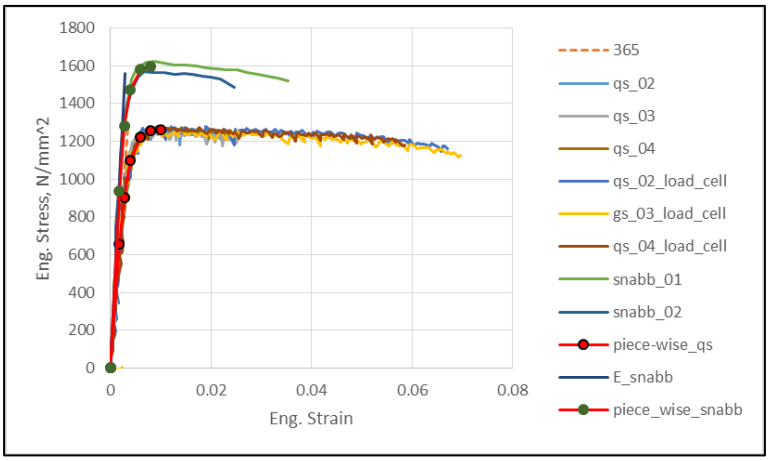

Figure 32: Experimental engineering stress as a function of the engineering strain for different loading rate

The tension tests shows that Y925 is rather sensitive to the strain rate even at moderate values. At strain rate of about 3.5 s^{-1}, the ultimate strength increases significantly from about 1300 MPa to about 1600 MPa. This is more than 23 percent increase in the strength. The failure strain reduces significantly at the increased strain rate, from about 0.07 to 0.03. The measured Young's modulus is 365 GPa for the quasi-static load, which is slight higher than the value from [19]. It becomes 540 GPa at the strain rate of 3.5 s^{-1}, indicate a strong viscosity effect of the material.

To investigate the strain rate sensitivity at an even higher strain rate, the pendulum single bar Hopkinson impactor test apparatus has been used [18]. This test apparatus has the benefit of using the same smooth specimen (Fig.31) for the quasi-static tension test at a strain rate up to several hundred strain per second. In addition to the studying of the strain hardening effect, the test apparatus provides results for the dynamic failure strain that are essential for the determination of the fracture. The apparatus can load the specimen with a strain rate in the order of 10^2 s^{-1} which is between the hydraulic servo testing machine and the rate by the split-Hopkinson pressure bar (SHPB) apparatus.

The disadvantage of the pendulum test apparatus is the difficulty to translate and understand the test results since the dynamics load due to the impact shock is very complicated. The hybrid method has again to be used to understand the test results and determine material parameters from the recording.

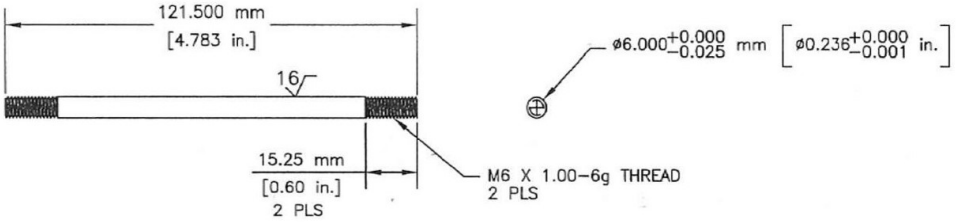

Figure 33: Dimension of the smooth specimen for the tension tests of Y925 at elevated temperatures

To provide material data for elevated temperatures, some quasi-static tension tests have been performed [20] for the temperatures up to 1500 °C (1773 K), which is near the melting temperature of the matrix of the alloy. For these temperature tests, larger specimens are used. The dimension of the specimen is shown in Fig.33. For the elevated temperature tests, the gripping area is outside of the oven so that there is no reason to

increase the size in the gripping section to ensure the failure to occur in the gauge section of the specimen.

Some examples of the test results are shown in Fig.34 for the stresses as a function of the strain. In comparison, the quasi-static tests at room temperature is shown in the figure as the dark red curve. These test data will be used to determine the temperature softening parameters for both the strength and the fracture model of Y925 alloy.

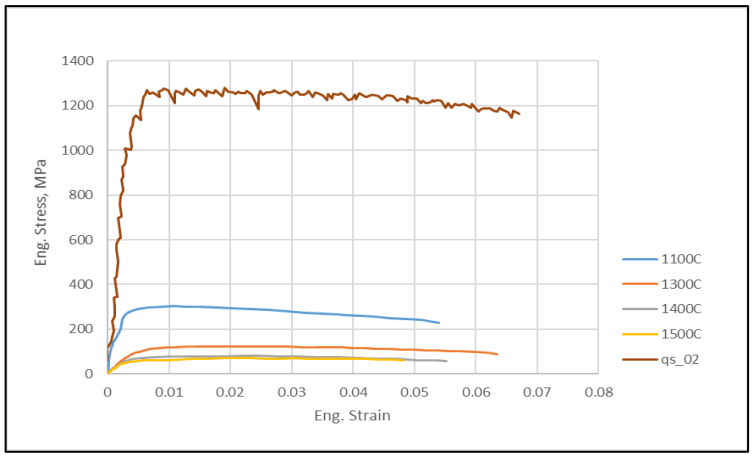

Figure 34: The quasi-static test results of the stress as a function of strain at elevated temperatures

7.2 Strain and strain rate hardening

A numerical model is created for the tension test with the smooth specimen. To create a reasonable model, a convergence study was again performed since this material is significantly different from S355J2.

While a general convergence will be reached with rather large element size before the load has reached the maximum value, the behavior after the maximum load will be mesh size sensitive due to the necking (plastic instability) of the specimen. Since this study concerns the failure behavior, it is decided that an element size of 0.035 mm is needed for the simulation of the failure of this material with a reasonable convergence for the axial load as a function of deformation.

Since the parameters for some of the strength models have been established previously, it is essential to validate them with the new test data since the material for the present study comes from a different batch.

For the tension tests, a comparison of the simulated results according to different parameter sets is shown in Fig.35 for both the quasi-static and the increased strain rate tests. The comparison shows that while the previous parameters from [5] for a similar material denomination (Y925) have a reasonable agreement with the quasi-static test results as shown in the figure as the green dotted curves (denoted as ‘peter’ in the figure), the model agrees poorly with the results at the increased strain rate. The widely used parameters from Johnson and Cook (denoted as JC in the figure) agrees poorly with the quasi-static test results as shown as the red dashed curves. Its performance at the increased strain rate seems to be excellent, see Fig.35.

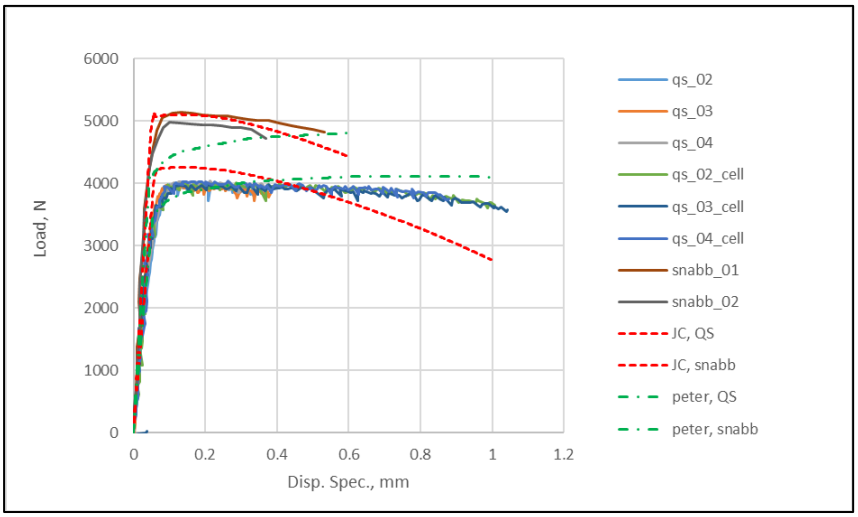

Figure 35: Comparison of various strength models to the test results for the quasi-static test and the test at elevated strain rate

At even higher strain rate, a comparison of the simulated and the test results from the pendulum Hopkinson impactor test is shown in Fig.36. In this figure, the symbols are the test recordings of the strain on the Hopkinson bar [2], and the symbols are the simulations with different sets of parameters for JC model. Again, the validation shows that the parameters from original Johnson-Cook's research gives a rather satisfactory agreement with the test results while the parameters from the study from [5] will underestimate the strain rate hardening of the material (the green curve). It becomes obvious that an improved set of parameters for JC model for this material is needed to describe the material behavior of the Y925 tungsten alloy (the black curve).

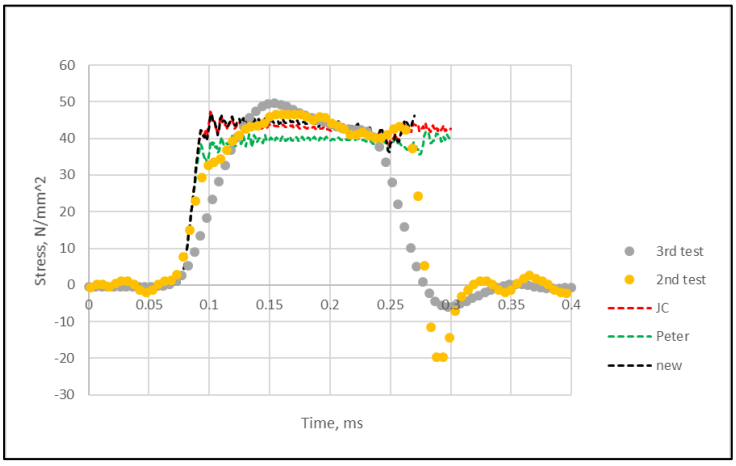

Figure 36: Comparison of the strain response during the pendulum Hopkinson tests for the stress at the measurement location

To determine parameters for the strength model as given in Eq. (14), the quasi-static test results, the strain rate test results, as well as the temperature test results are considered. According to the temperature test results as shown in Fig.37 and from [5] and [20], the maximum engineering stress as a function of the temperature is shown in Fig.37 for the quasi-static loading condition. Based on these results, the temperature constant in the strength model is estimated to be $m = 0.9$ for a reference melt temperature of $T_m = 1728\ K$ (the melt temperature of the matrix), see Fig.37.

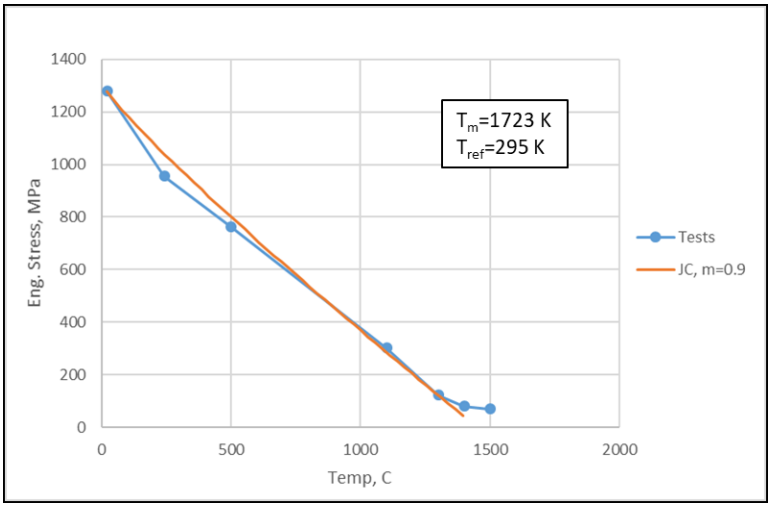

Figure 37: Comparison of the reduction of the maximum stress as a function of the temperature

Similarly, the engineering failure strain as a function of the temperature is estimated from these test data and the results are shown in Fig.38. In this figure, the symbols are the test data. A linear fit to these data results in a failure constant $D_5 = -0.17$ for the failure model of Eq. (17). Clearly this material will fail at a less critical strain at the elevated temperature.

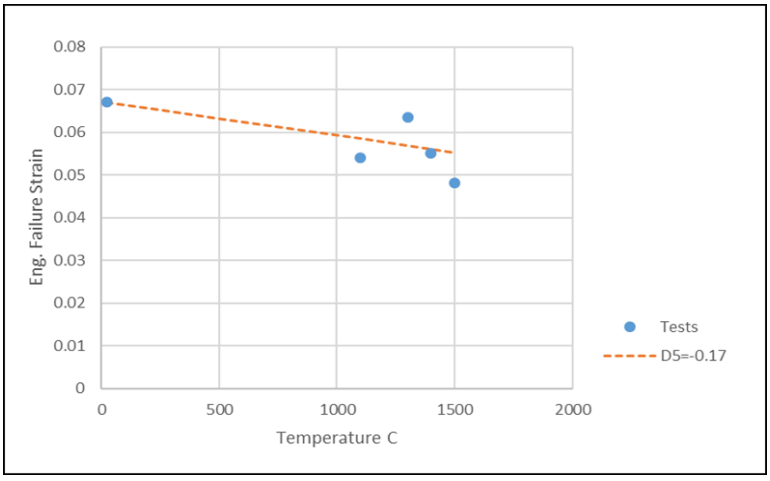

Figure 38: The experimental engineering failure strength as a function of the temperature

A piecewise representation of the true stress-strain relation can be determined from the tension tests with the smooth specimens as the results shows in Fig.32 as symbols. The results are shown in Table 3 for the quasi-static loading condition.

Table 3: Quasi-static (10^{-4} s^{-1}) piecewise linear data for Y925

Plastic	***Stress***
Strain	*Mpa*
0.0000	*0.0*
0.0000	*658.2*
0.0003	*902.5*
0.0010	*1104.4*
0.0026	*1227.3*
0.0045	*1265.0*
0.0065	*1272.6*
0.1000	*1370.0*

Simulations with parameters for the quasi-static condition are performed for the condition at the increased strain rate to determine the dynamic increasing factor (DIF). An example of the strain rate test from the hydraulic testing machine is shown in Fig.39. In this case, a DIF is applied on the parameters of the quasi-static strength model for the dynamic loading condition such that an optimum agreement with the test results is achieved.

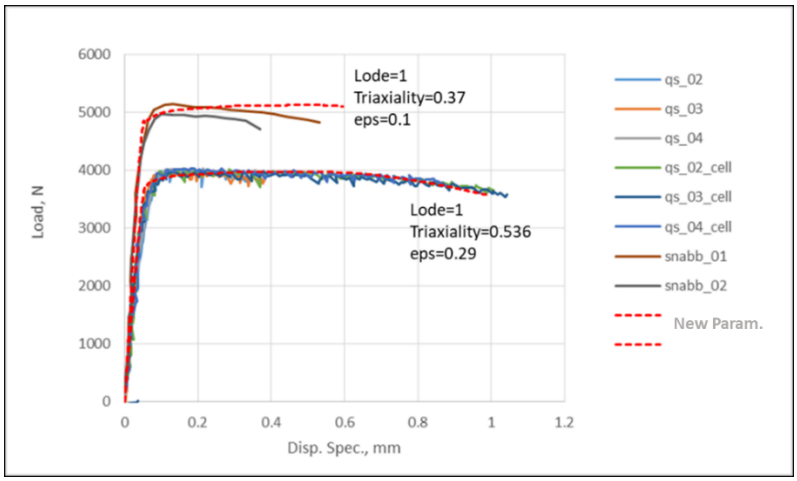

Figure 39: Comparison of the simulations with the test results for determination of DIF the loading at elevated strain rate

The same procedure is used to evaluate DIF from the pendulum Hopkinson impact tests. The optimum result of the simulation is shown in Fig.40. In this figure, the symbols are the test recordings of the stress on the Hopkinson bar, and the red dashed curve is the simulation result from the new parameters. In this figure, the failure condition is identified and shown in the insert for the critical strain and the corresponding stress triaxiality and Lode parameters at failure.

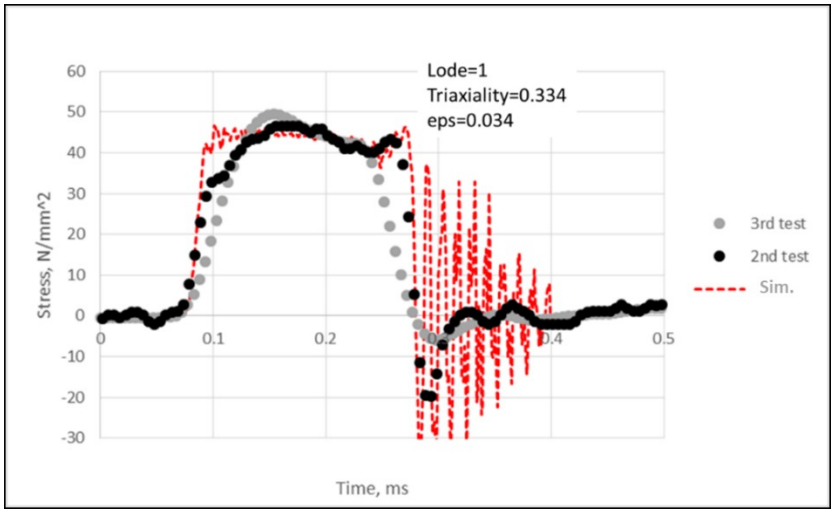

Figure 40: Simulation of the stress on the Hopkinson bar for the pendulum impact tests, compared to the measurements

The DIFs determined with the hybrid method for the strain rate tests are compared in Fig.41. In this figure, the DIF is shown as a function of the strain rate in a logarithmic scale. A linear fit to these data results in a constant $C = 0.022$ for the strength model of Eq. (14).

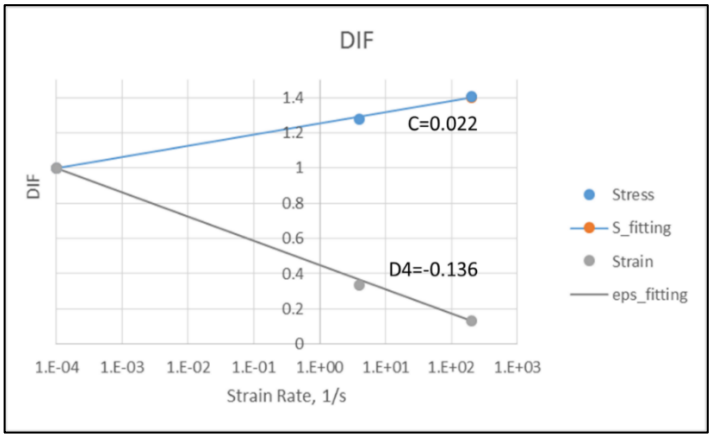

Figure 41: DIF determined with the hybrid model for the material testing results

Accordingly, a new set of parameters for the strength model in MPa is determined for Y925 as:

$$\sigma_y(\varepsilon_p, \dot{\varepsilon}_p, T) = \left[1028.6 + 458.7(\varepsilon_p)^{0.14}\right][1 + 0.022ln(|\dot{\varepsilon}^*|)][1 - (T^*)^{0.9}] \quad (52)$$

The model is referred to a reference strain rate of $\dot{\varepsilon}_0 = 10^{-4}\ s^{-1}$. The value is closely related to the quasi static loading rate of $\dot{\varepsilon}_0 = 2.5 \times 10^{-4}\ s^{-1}$ specified in ISO 6892-2:2018.

7.3 Fracture strain

The available material for Y925 is cylindrical bars with diameters of either 6 mm or 8 mm. With this size, it is not feasible to produce hollow cylinder specimens for the material tests. A new strategy has to be considered for the tests to provide fracture data for the

stress states such as shear and plane strain condition. For this purpose, some of special designs of specimens are considered.

7.3.1 Fracture tests

In addition to the smooth specimens as shown in Fig.31, a deep notch specimen configuration has been considered based on numerical simulations. Due to the limitation of the size of the raw material, the notched specimen has become a practical candidate. Differing from the tests with large notched specimens that are used to create a high stress triaxiality in the center of the fracture section, these tests will put more emphasis on the Lode parameter dependency of the notched specimen.

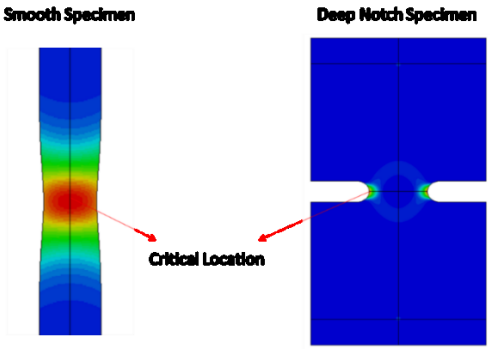

Figure 42: Comparison of critical condition between the deep notch and smooth tension specimen

The idea is to size the specimen to force the initiation of fracture from the center to the surface of the notch. In this way, a different failure condition can be created. The configuration of the specimen is shown in Fig.43. With an excessive depth of the notch and a small notch radius, it is possible to force the initiation of failure from inside of the gauge section towards the surface of the notch. As a result, the stress triaxiality and Lode parameter will become significantly different from that of the large notch specimens for which the initiation of the fracture will occur at the center of the specimen, see the comparison as shown in Fig.42.

The dimensions of the specimen are shown in Fig.43. For this specimen, the radius of the notch is R0.4 mm and the diameter of the critical section is 1/3 of the outer diameter. The outer diameter is 7.5 times larger than the notch width, see Fig.43. The tolerance control of the specimens is focused on the notch width and the notch diameter, see Fig.43. No control of notch surface condition is performed since the goal is to study the bulk property. It was considered that the surface roughness may play a secondary role under the condition of large plastic deformation. This test is one of the steps to experimentally determine the fracture strain at a different stress state.

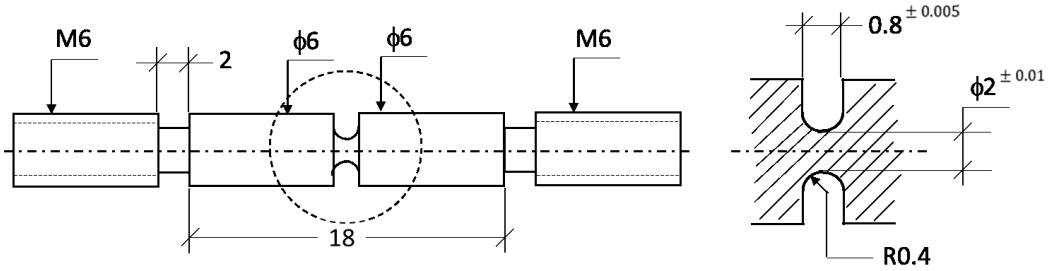

Figure 43: Dimensions of the deep notch tension specimen

Again, a convergence study has to be performed to determine the numerical model since the specimen geometry is significantly different from the smooth specimen. From the convergence study, the element size of 0.015 mm is chosen for the numerical model in the critical section.

Simulations are performed for the test and compared in Fig.44 for the applied load as a function of the displacement in the gauge section. In this case, the gauge distance is 10 mm, symmetrically across the notch section.

Since the simulation is based on parameters determined by the tension tests with smooth specimens, some discrepancy have been observed between the simulated responses of the applied load as a function of the displacement in the gauge area as the comparison shows in Fig.44. It is decided to rely on the simulation to determine the failure strains.

The failure condition determined with the simulations is shown in the insert of Fig.44. The result shows that the critical strain is about 0.03, which is significantly lower than that of the smooth specimen. The stress triaxiality seems to be similar (0.572 for the notch specimen and 0.536 for the smooth specimen). The difference is in the Lode parameter. For the smooth specimens, the Lode parameter is close to 1, while for the deep notch specimen, the Lode parameter is around 0.325.

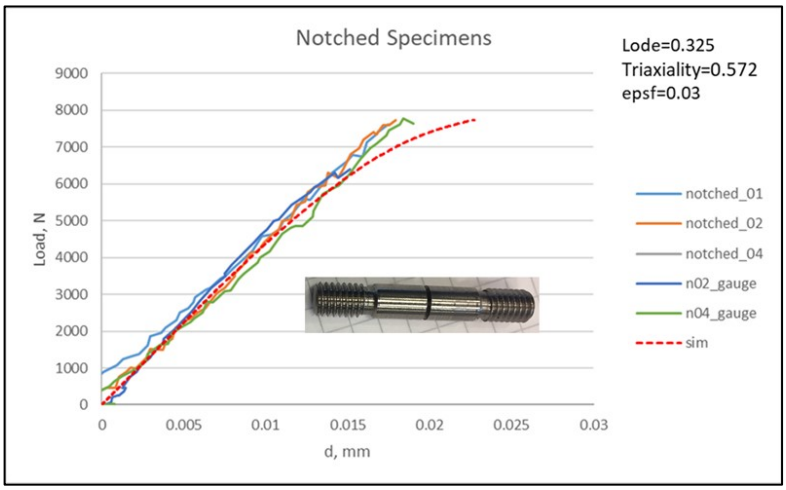

Figure 44: Comparison of the test and the simulation results for the applied load as a function of gauge displacement

To consider the failure strain as a function of stress triaxiality, a comparison is shown in Fig.45 for results from the smooth specimen and the deep notch specimen. In this figure, the average results from the test are shown as the symbols. It is shown that there is significant difference in the failure strain between the test results. This is a strong indication of the shortcoming of JC failure model for this material.

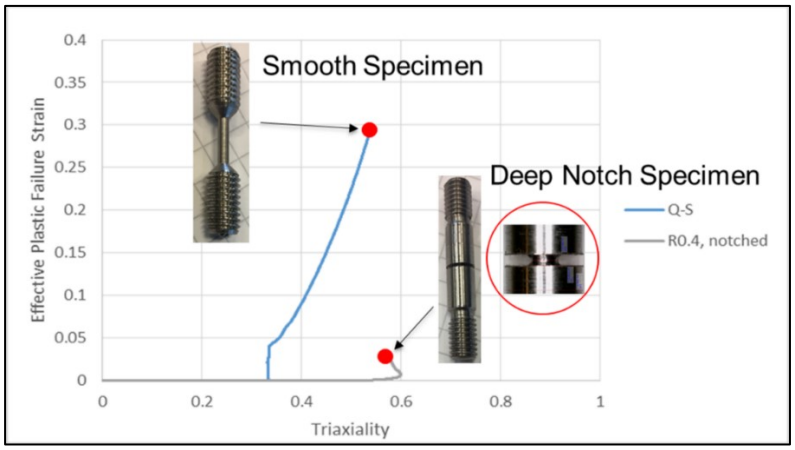

Figure 45: Comparison of the failure strain determined by the hybrid method as a function of stress triaxiality between the smooth specimen and the deep notch specimen

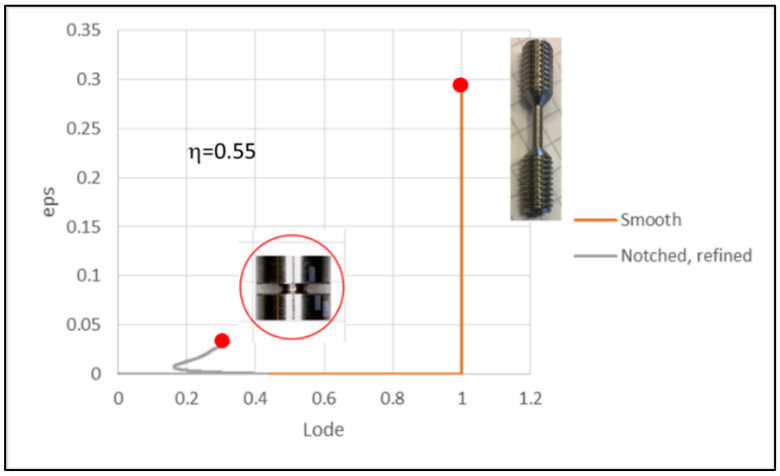

Figure 46: Comparison of the failure strain determined by the hybrid method as a function of the Lode parameter between the smooth and deep notch tension tests

When the failure strain is expressed as a function of Lode parameter, as shown in Fig.46, its dependency on the Lode parameter becomes clear, indicating that the failure model of Y925 has to include the effect of Lode parameter.

To create a failure condition under a negative stress triaxiality means to find a way to break the material under a compressive stress condition. Compression tests with smooth cylinder specimen is obviously out of question for most metallic materials that can withstand significant plastic deformation under compression. Unlike brittle materials, the compression seldom creates an adiabatic shear band failure.

A forced shear solution is considered. With a button design as shown in Fig.47, a compression load is applied on the top of the button to create a shear in the middle section of the button. If one sizes the plug of the button with a slightly larger diameter than that of the hole, the plug will be forced into the smaller hole during compression and, thus, create a normal compression stress in the shear band to achieve the desired stress state. As a result, a shear failure may be initiated at negative stress triaxiality.

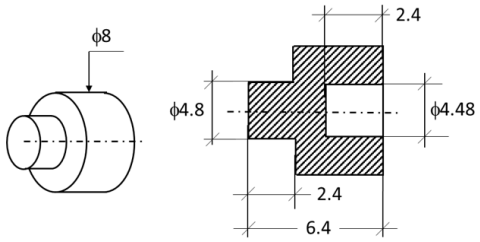

Figure 47: Dimensions of the forced shear compression button specimen.

With the forced shear button, several compression tests have been performed. The test results is shown in Fig.48 for the applied force as a function of the displacement of the supporting plates. As shown in the test results in Fig.48, there is a considerable residual load even after the failure when the oversized plug is forced into the smaller hole. The interference of the plug and hole will lead to a significant frictional force, see Fig.48.

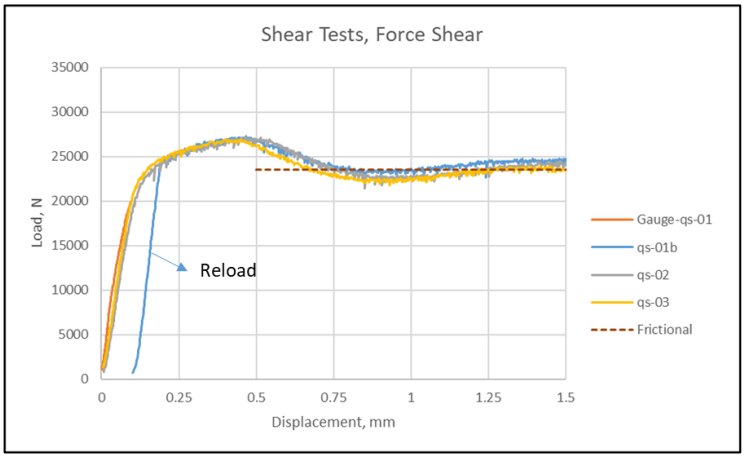

Figure 48: Test results of the applied load as function of the displacement of the platforms for the forced shear tests of Y925

To determine the failure condition, numerical simulations are necessary. A convergence study has to be performed to determine the size of the element in the critical section. For the button specimen, it is found that the reaction load will be very sensitive to the mesh size after the maximum load has been passed when excessive plastic deformation occurs. According to the mesh sensitivity study, a mesh size of 0.05 mm is required for a reasonably converged result.

For this specimen, the simulations showed that failure of the specimen seems to become progressive. There is no clear break point when failure occurs. There will be a great uncertainty in identifying the critical location and value. The load level and stress state for failure are not clearly defined. Unlike the tension specimens that shows an abrupt loss of strength after the initiation of failure, there will still be a significant load increase after the initial failure. An engineering approach is thus adopted to estimate an average failure condition for this specimen.

Trial-and-error simulations were performed for different assumptions of the failure strain until the simulated load-displacement response has an acceptable agreement with the test result. The final result is shown in Fig.49 for a comparison between the simulation and the test results. This figure shows the result of simulation without failure strain (the brown dashed curve), compared to the simulation with an acceptable failure strain assumption (the grey dashed curve). The average failure condition from the simulation is shown in the insert. The hybrid method shows that there appears to be a high average negative

(compressive) stress triaxiality (-1) at a near shear condition (Lode=0.02). For this condition, the failure will occur at a rather large value of average strain (2.5).

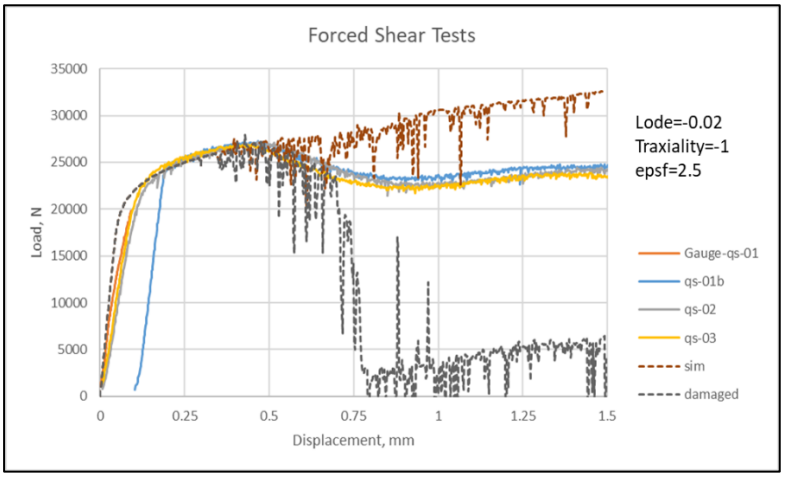

Figure 49: Comparison of the results from tests and simulations for identifying the failure condition of the forced shear specimens.

8 Conclusions

In this study, extensive efforts have been made to characterize the dynamic and failure properties of S355J2 and Y925. The activity includes design of material tests and hybrid analyses of the test results. A system method is used to analyze the dynamic response of the tests at high strain rate using the Hopkinson single bar impactor and the Kosky split bar apparatus. With the help of simulations, it is shown that critical material parameters may be identified with complex specimen designs for the failure conditions for different fracture patterns. These tests are essential for the development of advanced material models for ballistic applications.

Even with standard smooth specimens, it is shown that a complex stress state may be presented for many materials after the maximum load has been passed. Instead of use of the Bridgman's engineering method that requires tedious measurements of the dimensional change of the specimen during the tests after necking, the hybrid method has proved to be an effective alternative in determining the material parameters.

In addition to the complex tests by biaxial load that have been developed in [1], two new types of specimen designs have been explored in this study with successful results for small material samples. These types of specimens require only uniaxial load for the tests to determine the failure parameters in shear and compression.

With the hybrid methods, parameters for an advanced failure model, the Hosford-Mohr-Coulomb model, have been studied and the method to determine the material parameters of the model has been explored.

In summary, the parameters for JC strain hardening law in the expression of Eq. (14) are determined and validated with the test results respectively for S355J2 and Y925. Table 4 shows a summary of the parameters for JC models. These parameters are valid for large plastic deformation after the geometrical instability (*i.e.* necking).

Table 4: The parameters for the JC strain hardening model

Material	*A*	*B*	*n*	*C*	*m*	*eps0*	T_{ref}	T_m	C_p
	MPa	*MPa*				*1/s*	*K*	*K*	*J/kg-K*
Y925	1028.6	458.7	0.14	0.0220	0.9	10^{-4}	293	1728	150
S355J2, annealed	11.2	754.8	0.16	0.0145	1.1	10^{-4}	293	1793	452
S355J2, rolled	12.8	881.0	0.16	0.0145	1.1	10^{-4}	293	1793	452
S355J2, drawn	13.1	883.1	0.11	0.0145	1.1	10^{-4}	293	1793	452

The parameters for the equivalent JC failure model of Eq. (17) are given in Table 5. The corresponding JC failure model is defined in Eq. (53).

$$\varepsilon_f^p = (D_1 + D_2 e^{D_3 \eta})(1 + D_4 ln|\dot{\varepsilon}^*|)(1 + D_5 T^*) \quad (53)$$

Table 5: Equivalent constants for JC failure model

Material	D_1	D_2	D_3	D_4	D_5
S355J2, annealed	0.07	1.60	-1.50	0	0
S355J2, rolled	0.05	1.47	-1.63	0	0
S355J2, drawn	0.03	1.35	-1.75	0	0

The parameters for HMC failure model under the quasi-static loading condition are determined and shown in Table 6 for S355J2.

Table 6: Constants for the HMC model for different conditions of S355J2 at quasi-static loading condition

Material	ε_0	a	c	nf
S355J2, annealed	1.015	2.829	0.118	0.16
S355J2, drawn	0.767	2.767	0.097	0.11

The fracture tests for Y925 indicate its strong Lode parameter dependency. At the present state, only the yield model is presented and validated for the tension condition. Further effort is required to verify whether or not the von-Mises yield is a proper assumption, and more fracture tests and validations are needed to populate the fracture locus for the development of a reliable fracture model for this material.

9 Acknowledgement

Financial support from FM, Swedish Armed Force, is gratefully acknowledged for this study.

10 References

[1] G. S. Wang, “Characterization of Strength and Fracture Properties of S355-J2 Steel”, FOI-R--4470--SE, nov. 2017.

[2] G. S. Wang, “Hybrid Method to Characterize Dynamic Material Parameters from Split Hopkinson Pressure Bar Test”, FOI-R--4527--SE, 2017.

[3] S. Leonardsson, “Quasistic tensile testing with image analysis for structural steel S355J2”, Master’s Thesis in Physics, Umeå University, FOI-R-3257--SE, Dec. 2011.

[4] S. Mousavi, and S., Leonardsson, “S355J2 Dynamic and Static material tests for UNDEX experiments”, FOI-R--3454--SE, July 2012.

[5] P. Skoglund, “Constitutive modelling and mechanical properties of a tungsten heavy metal alloy”, FOI-R--0723--SE, Nov. 2002, Swedish Defence Research Agency.

[6] A. Tjernberg and P. Skoglund, “Brottparametrar för en volframlegering”, FOI-R--2283--SE. April 2007, Swedish defence research agency.

[7] W. Lode, Versuche über den Einfuss der mittleren Hauptspannung auf das Fliessen der Metalle Eisen Kupfer und Nickel. Zeitung Phys., vol. 36, pp. 913–939. 1926.

[8] Hosford, W.F., 1972. A generalized isotropic yield criterion. J. Appl. Mech. 39, 607.

[9] G.R. Johnson, W.H. Cook, 1983. A constitutive model and data for metals subjected to large strains, high strain rates and high temperatures. In: Proc. 7th International Symposium on Ballistics, pp. 541–547.

[10] G.R. Johnson and W.H. Cook, Fracture characteristics of three metals subjected to various strains, strain rates, temperatures and pressures, Eng. Frac. Mech. V.21, pp.31-48, 1985.

[11] Y. Bai, T. Wierzbicki, Application of extended Mohr-Coulomb criterion to ductile fracture. Int. J. of Plasticity, v.161, pp.1-20, 2010.

[12] S. Bernhardsson och O. Andersson, “Numerisk studie av penetration i pansarstål”, FOI-R- -3873- -SE, June, 2014.

[13] G. S. Wang, P. Appelgren, M. Ingvarsson, , U. Widing and P. Lundberg, “Ballistic Performance of High Strength Steel and Aluminum Plates Against Spherical Tungsten Fragments”, In: Proc. 31th International Symposium on Ballistics, pp.1341-1352, Hyderabad, India, nov. 2019.

[14] C.A. Coulomb, Essai sur une application des règles des maximis et minimis à quelques problèmes de statique relatifs à l’architecture. Mem. Acad. Roy. Div. Sav. 7, 343–387. 1776.

[15] D. Mohr and S. J. Marcadet, “Micromechanically-motivated phenomenological Hosford–Coulomb model for predicting ductile fracture initiation at low stress triaxialities”, Int. J. of Solids and Struc. V.67–68, 15 August 2015, pp.40-55.

[16] M. A. Meyers, Dynamic behavior of materials: John Wiley & Sons, Inc., 1994 D. A. S. Macdougall and J. Harding, “The measurement of specimen surface temperature in high-speed tension and torsion tests”, Int. J. of Impact Engng, v.21, p.473, 1998.

[17] J. Outinen and P. Mäkeläinen, Mechanical properties of structural steel at elevated temperatures and after cooling down. Second International Workshop « Structures in Fire », Laboratory of Steel Structures, Department of Civil and Environmental Engineering, Helsinki University of Technology, Finland, 2002.

[18] T. Svensson, “A pendulum impactor for confident tensile testing at high rates of strain”, National defence research institute, Stockholm, FOA report C 20577-D4, June 1985.

[19] L. S. Magness, “A phenomenological investigation of the behavior of high-density materials under the high pressure, high strain rate loading environment of ballistic impact”, Dissertation, John Hopkins University, Baltimore, Maryland, 1992.

[20] Johan Eliasson and Johan Lönnqvist, “Tensile testing at high temperatures of a W-material”, Feb. 2018. Swerea/Kimab, Lab. Report, reference no.: TMPA20171026-1.

FOI, Swedish Defence Research Agency, is a mainly assignment-funded agency under the Ministry of Defence. The core activities are research, method and technology development, as well as studies conducted in the interests of Swedish defence and the safety and security of society. The organisation employs approximately 1000 personnel of whom about 800 are scientists. This makes FOI Sweden's largest research institute. FOI gives its customers access to leading-edge expertise in a large number of fields such as security policy studies, defence and security related analyses, the assessment of various types of threat, systems for control and management of crises, protection against and management of hazardous substances, IT security and the potential offered by new sensors.

FOI
Defence Research Agency
SE-164 90 Stockholm

Phone: +46 8 555 030 00
Fax: +46 8 555 031 00

www.foi.se